Stacking of interferometric data - a submillimetre and radio view on the evolution of distant galaxies

LUKAS LINDROOS

Stacking of interferometric data - a submillimetre and radio view on the evolution of distant galaxies
LUKAS LINDROOS

Radio Astronomy & Astrophysics Group
Department of Earth and Space Sciences
Chalmers University of Technology
SE–412 96 Göteborg, Sweden
Phone: +46 (0)31–772 1000

Contact information:
Lukas Lindroos
Onsala Space Observatory
Chalmers University of Technology
SE–439 92 Onsala, Sweden

Phone: +46 (0)31–772 5543
Email: lukas.lindroos@chalmers.se

Cover image:
The Hubble Ultra Deep Field, composite image showing the visible and near infrared light. Created for NASA by Space Telescope Science Institute under Contract NAS5-26555.

Stacking of interferometric data - a submillimetre and radio view on the evolution of distant galaxies

Lukas Lindroos
Department of Earth and Space Sciences
Chalmers University of Technology

Abstract

Understanding the processes of galaxy evolution requires observational constraints on the physical properties of galaxies at different times in the history of the universe. Large and deep surveys at visible and near-infrared wavelengths have produced extensive catalogues of high-redshift galaxies, spanning a large range of the history of the universe. Over this time the galaxies undergo significant evolution, increasing not ooly their stellar content, but also their physical size. In this thesis I will present results from observations of star-forming galaxies at submm and radio wavelengths. Observations at these longer wavelengths probe young stars, showing where new stars are formed in the galaxies. The observations presented in this thesis show that, for star-forming galaxies out to $z \approx 3$, the sizes measured at submm and radio wavelengths are significantly smaller than those measured at near-infrared wavelengths. This implies that most stars are formed in the centre of galaxies, indicating that in the absence of other size evolution mechanisms we expect the typical effective radii of galaxies to decrease with time. It highlights the need for other size evolution mechanisms, such as minor mergers or changes in the galaxies due to stellar feedback.

A major part of this thesis investigates the technique of stacking for interferometric data. Stacking is a technique to study statistical properties of populations, and is currently essential for the study of high-redshift, star-forming galaxies at submm and radio wavelengths, as many of high-redshift galaxies are too faint to be observed directly. Typically, stacking at different wavelengths ranges is done using deep imaging surveys observed with a single telescope. However, interferometry is not a direct imaging technique, and this presents a number of challenges to stacking. We present a new stacking algorithm that works directly on the visibilities; we refer to it as uv-stacking. We compare this algorithm to an image-stacking algorithm, i.e., an algorithm that stacks the sources directly in the imaged data. The uv-stacking algorithm is found to yield more robust results than the image-stacking algorithm. It is of particular interest for size measurement of stacked galaxies, as it preserves the uv data through stacking, and allows for robust model fitting of the stacked data.

Keywords: techniques: interferometric – methods: data analysis – galaxies: high- redshift – radio continuum: galaxies – sub-millimetre: galaxies

Research contributions

This thesis is based on work described in the following papers.

I L. Lindroos, K. K. Knudsen, W. Vlemmings, J. Conway, & I. Martí-Vidal:
Stacking of large interferometric data sets in the image- and uv-domain – a comparative study
Monthly Notices of the Royal Astronomical Society, Volume 446, Issue 4 (2015)

II L. Lindroos, K. K. Knudsen, L. Fan, J. Conway, K. Coppin, R. Decarli, G. Drouart, J. A. Hodge, A. Karim, J. M. Simpson, and J. Wardlow:
Estimating sizes of faint, distant galaxies in the submillimetre regime
Submitted to Monthly Notices of the Royal Astronomical Society.

III L. Lindroos, K. K. Knudsen, T. W. B. Muxlow, R. J. Beswick, J. Conway, J. F. Radcliffe, and N. Wrigley: *Measuring size evolution of faint, distant galaxies in the radio regime*
Manuscript intended for Monthly Notices of the Royal Astronomical Society

I have also participated in the following paper not included in the thesis:

- R. Decarli, I. Smail, F. Walter, A. M. Swinbank, T. R. Greve, J. A. Hodge, R. Ivison, A. Karim, K. K. Knudsen, L. Lindroos, H. W. Rix, E. Schinnerer, J. M. Simpson, P. van der Werf, and A. Weiß:
An ALMA Survey of Sub-millimeter Galaxies in the Extended Chandra Deep Field South: Sub-millimeter Properties of Color-selected Galaxies
The Astrophysical Journal, Volume 780, Issue 2 (2014)

- S. König, S. Aalto, L. Lindroos, J. S. Gallagher, R. J. Beswick, G. Petipas, and E. Jütte:
Molecular tendrils feeding star formation in the Eye of the Medusa. The Medusa merger in high resolution ^{12}CO 2-1 maps
Astronomy & Astrophysics, Volume 569 (2014)

- K. K. Knudsen, J. Richard, J.-P. Kneib, M. Jauzac, B. Clement, G. Drouart, E. Egami, and L. Lindroos:
[CII] emission in $z \sim 6$ strongly lensed, star-forming galaxies
Accepted for publication in Monthly Notices of the Royal Astronomical Society

Acknowledgements

Contents

Chapter 1

Introduction

When we are looking out into space, we are also looking back in time. The light from distant parts of the universe, arriving at Earth today, has travelled for billions of years. From the edges of the visible universe, comes the cosmic microwave background radiation, telling us that at early times the universe was extremely homogeneous (e.g. Planck Collaboration et al. 2014). Today the picture is very different: Almost all light is emitted from galaxies, dense clumps of stars and gas. The field of *galaxy formation and evolution* aims to understand this transformation of the universe. From the first seeds all the way to present-day galaxies.

The further away a galaxy is, the more the light has been reddened by the expansion of the universe, often quantified in terms of the redshift (z).[1] Using modern telescopes, galaxies have been detected across a wide range of redshifts, with many galaxies detected at $z \approx 7$ (e.g. Finkelstein et al. 2013; Song et al. 2016; Bian et al. 2015; Oesch et al. 2015) and some detections as far away as $z \approx 11.1$ (Oesch et al. 2016). This corresponds to light emitted when the universe was 700 and 400 million years old.[2] Observations of galaxies at different redshifts indicate that in total relatively few stars are formed at these early times. Studying galaxies closer than $z \approx 7$, the star formation rate in a given volume of space (star-formation rate density) quickly picks up and reaches a peak between redshift 2 and 3 (e.g. Bouwens et al. 2011; Madau & Dickinson 2014) or 2-3 billion years after the Big Bang. After the peak, the star-formation rate density decreases, and appears to be still dropping today.

The general frame work of galaxy formation and evolution is set by our cos-

---

[1]The redshift is defined as the ratio between the change in wavelength and the original wavelength, i.e., $z = \frac{\lambda_{\mathrm{obs}} - \lambda_0}{\lambda_0}$ where λ_{obs} is the wavelength of the light today, and λ_0 is the wavelength when the light was emitted.

[2]In this thesis I assume a flat universe with $H_0 = 67.3$ km s^{-1}, $\Omega_\Lambda = 0.685$, and $\Omega_M = 0.315$ (Planck Collaboration et al. 2014).

mological model. The currently accepted cosmological model (called ΛCDM), dictates that the universe at early times was dominated by cold dark matter, a matter consisting of massive particles that interact only through gravitation. Through the process of inflation, where the universe rapidly increased its size, small quantum perturbations in the dark matter form larger overdensities that grow into dark matter halos. In these dark matter halos baryonic gas is gathered. This gas cools through radiation and collapses to form regions dense enough to start forming stars. These systems of gas and stars grow, either through merging with other systems, or by accreting loose baryonic gas, to form the galaxy zoo of today.

While this model describes the general trends well, there are many details in this picture that are still uncertain. Many unanswered questions remain, such as: What is the role of mergers versus the role of secular evolution, i.e. galaxies forming stars at a steady rate, being fed by streams of gas from the intergalactic medium? Is star formation constant or does it happen in bursts? What internal mechanisms regulate star formation in galaxies?

1.1   This thesis

The main aim of this thesis is to address the following two questions: "What does the size evolution of star-forming galaxies look like at submm and radio wavelengths?" and "How do we best perform stacking for interferometric data?"

Much work has been focused on understanding the size evolution of galaxies using the Hubble Space Telescope (*HST*). Such *HST* studies allow us to understand how the stellar component of galaxies evolve and show a strong growth over redshift. However, this growth is far from fully understood. By measuring the size evolution at submm and radio wavelengths we can directly probe where in the galaxies new stars are formed. This allows us to understand the importance of new stars as a driver of size evolution, in particular in regard to inside-out growth of galaxies.

The second question is related to the first, as we use stacking to measure the sizes of galaxies, but it is also an important question in itself. Stacking of interferometric data is not straightforward, and in this thesis much effort has been spent to ensure that the newly developed methods are robust. These techniques can be used in a wide range of different applications, and are not limited to the study of high-redshift galaxies.

The thesis includes three appended papers. Paper I introduces a new algorithm for stacking of interferometric data. This algorithm works in the *uv*-domain in contrast to older methods that work in the image-domain. Paper II shows how the *uv*-stacking algorithm can be used with ALMA data to measure

the sizes of star-forming galaxies at $z \sim 2$. Paper III uses data from MERLIN and VLA to measure the size evolution of star-forming galaxies at radio wavelengths, from the local universe to $z \sim 3$.

This thesis is structured as follows. The first chapter offers a general introduction of galaxies at high and low redshift. The second chapter introduces stacking, with an in-depth discussion of stacking of interferometric data, introducing and expanding on Paper I. The third chapter relates to statistical techniques for robust estimation of average properties of populations. The final and fourth chapter discusses the size evolution of high-redshift galaxies. This chapter introduces Paper II and Paper III, which concern the size evolution at submm and radio wavelengths, respectively.

1.2 Galaxies in the local universe

General reference: Sparke & Gallagher (2007); Conselice et al. (2014)
With the advent of photography in the early 20th century it became possible to study large numbers of the nearby galaxies. This sparked a general effort to categorize the galaxies. Most famous of these classifications is probably the Hubble sequence, proposed by Hubble (1926). This classification divides galaxies into four different types: elliptical, spiral, lenticular, and irregular. *Spiral* galaxies are highly recognisable due to their spiral arms, such as the Andromeda galaxy shown in Fig. 1.2. Spiral galaxies have a rapidly rotating disk and generally also have a more spherical bulge in the centre. Depending on the mass of the bulge compared to the disk, spiral galaxies are classified from Sa to Sd, where Sa have the smallest bulges. In the centre of many spiral galaxies the spiral arms are replaced by one or several bars. Spiral galaxies with bars are often classified in a separate sequence from SBa to SBd. *Elliptical* galaxies are smooth and generally featureless. They are supported by random motion and the total angular momentum is typically very small compared to spiral galaxies. Inside large clusters of galaxies ellipticals are significantly more common, and enormous so called cD galaxies often occupying the centre of the clusters. Such galaxies can be 100 times more luminous compared to the Milky Way. However, much smaller galaxies can also be elliptical, such as dwarf ellipticals (dE), which are very diffuse galaxies or compact ellipticals such as M32. The *lenticular* galaxies are similar to the elliptical galaxies in their lack of features such as spiral arms, however, they have a rotating disk. These galaxies are labelled as S0. The galaxies that do not fit into the other galaxy categories are clumped into the group called *irregulars*. Galaxies in this group are often mergers, where a collision have disrupted the structures of the precursor galaxies. The Hubble sequence is often arrayed with elliptical galaxies on the left, spiral galaxies on the right, and lenticular in the middle. The spiral galaxies are in turn arranged with Sa and

Figure 1.1: A typical spiral galaxy and a typical elliptical galaxy. (Left) Andromeda galaxy, typical spiral galaxy, picture by Adam Evans. (Right) Abell S0740, typical elliptical galaxy, picture from HST (NASA, ESA, and The Hubble Heritage Team (STScI/AURA)).

SBa towards the left. In this sequence it is common to refer to galaxies on the left as early type, and galaxies further to the right as late type. This is not an evolutionary sequence, and it does not imply that elliptical galaxies generally evolve into spiral galaxies. While potentially confusing, it it is still a common to refer to elliptical and lenticular galaxies as early-type galaxies (ETGs), and spiral and irregular galaxies as late-type galaxies.

The total mass of the stars in a galaxy is referred to as the stellar mass (M_*). Galaxies exist with a wide range of stellar masses, e.g., the survey of nearby galaxies by Consolandi et al. (2016) found galaxies with M_* all the way from $\sim 10^7$ M$_\odot$ to $\sim 5 \times 10^{11}$ M$_\odot$.[3] Our own Milky Way have $M_* \approx 5 \times 10^{10}$ M$_\odot$, but large local spirals can reach approximately twice that $\sim 10^{11}$ M$_\odot$. However, the most massive galaxies are almost exclusively elliptical galaxies. The lower mass limit is less solid. Firstly, diffuse low mass galaxies can be very difficult to detect as the typical surface brightness is very low, secondly, it can be a question of definition what is large enough to be considered a galaxy.

Apart from stars, galaxies also contain gas spread in the interstellar medium (primarily hydrogen). For local spiral galaxies the gas mass is typically $\sim 10\%$ of the stellar mass, while for elliptical and lenticular galaxies the ratio is typically much lower (e.g. Young et al. 2011). Gas is required for the formation of new stars, as such, we also find that spiral galaxies form new stars at a much higher rate compared to elliptical galaxies. This is often quantified in terms of the star-formation rate (SFR) defined as the mass of new stars formed per unit time. E.g.,

---

[3]Measured in units of the mass of our sun: M$_\odot \approx 1.99 \times 10^{30}$ kg.

a spiral galaxy with $M_* \approx 5 \times 10^{10}\,\mathrm{M_\odot}$, such as the Milky Way, will typically have an SFR of a few $\mathrm{M_\odot}$ per year. The massive stars are short lived, very luminous and much bluer compared to smaller stars, as such spiral galaxies are typically much bluer compared to elliptical and lenticular galaxies.

1.3   Galaxies at high redshift

General reference: Conselice et al. (2014)
The classification of nearby galaxies is generally based on the morphology of galaxies. There are several reasons why such a classification is complicated for higher redshift galaxies.[4] Firstly it is more difficult to obtain high resolution images of high-redshift galaxies. But even if galaxies are imaged with high resolution, high-redshift galaxies are often highly irregular. Observation of high-redshift galaxies indicate that the Hubble sequence is not in place for $z > 1$, and almost not existing at $z > 2$. Instead, high-redshift galaxies are typically grouped into star-forming and quiescent galaxies. Quiescent galaxies are characterised by little ongoing star formation and older stellar populations, while star-forming galaxies have much higher SFR and large populations of young newly formed stars. Patel et al. (2012) looked at the morphology of star-forming and quiescent galaxies at $z \sim 0.6 - 0.9$, and found that most star-forming galaxies are late-type galaxies, while most quiescent galaxies are early-type galaxies. As such the classifications are in many cases equivalent at redshifts where the Hubble sequence is in place, and the terms are sometimes used interchangeably.

In parallel to spirals, the colours of star-forming galaxies are typically bluer compared to quiescent galaxies. This results in a bimodal colour distribution for galaxies, which has been seen across a range of redshifts (e.g. Baldry et al. 2004; Faber et al. 2007; Brown et al. 2007). However, classifying galaxies in a simple blue or red scheme can be misleading. Some of the galaxies with the highest SFR are also very dusty, i.e., the galaxies have a dense interstellar medium with dust grain that absorb the blue light from young stars. This causes these galaxies to be very red when observed. Instead more complicated criteria are used to identify star-forming and quiescent galaxies, such as the UVJ selection, which will be discussed in section 1.5.4.

1.3.1   Star-forming galaxies

The SFR in star-forming galaxies has been found to correlate with M_*. This correlation is often referred to as the star-formation sequence or the main sequence sequence of star-forming galaxies. Depending on how galaxies are selected, and

---

[4]The term high redshift is rather vague and can refer to any galaxies that are far away enough that cosmological correction become important for observations. In this thesis the focus is primarily on galaxies in the range from 1 to 3.

how M_* and SFR are measured, the exact shape of the correlation varies. A few common parametrizations are shown in Fig. 1.2. The scatter in this correlation is large. Galaxies that lie significantly above the relation are sometimes referred to as starburst galaxies, e.g., Rodighiero et al. (2011) consider galaxies with SFR ~ 4 times the median SFR for a given M_* to be starbursts. However, starburst is a relative term and the definitions vary between different authors. Starburst galaxies do stick out due to their sometimes extreme SFR, e.g., the galaxies with the highest SFRs in Whitaker et al. (2014) data set can double their stellar mass in a few tens of Myr. Starburst galaxies are also relatively rare, e.g., Rodighiero et al. (2011) estimate that at $z \approx 2$ only $\sim$2% of star-forming galaxies are starbursts. This results in less than 10% of the star-formation rate density at $z \approx 2$ originating in starburst galaxies. In this work the primary focus is on the plurality of the galaxies, galaxies that lie on the star-formation sequence.

1.3.2 Quiescent galaxies

Quiescent galaxies are primarily defined by their low specific SFR (sSFR $= \frac{\text{SFR}}{M_*}$). In this work this we define this as the population of galaxies that fall significantly below the SFR-M_* correlation seen for star-forming galaxies, equivalent to other studies of high-redshift star-forming galaxies (e.g. Williams et al. 2009). Other terms are in use in the literature as well, such as *passive galaxies* (e.g. Ownsworth et al. 2016) or *red and dead galaxies* (e.g. Leslie et al. 2016). Confusingly, the terms passive and quiescent are used differently by authors studying high-redshift starburst galaxies, e.g., Hayward et al. (2012) refer to all galaxies that are not starburst as quiescently star-forming or quiescent galaxies.

Studies have found significant populations of massive ($M_* \sim 10^{11} \text{M}_\odot$) quiescent galaxies as far out as $z \sim 4$ (e.g. Straatman et al. 2014), despite the age of the universe only being 1.5 billion years at this point. The Straatman et al. (2014) results indicate that 34 ± 13 % of massive galaxies ($M_* > 10^{10.6} \text{M}_\odot$) at $z \sim 4$ are quiescent, compared to $\sim 80\%$ at $z \sim 0$.

1.4 Galaxy evolution

As is evident when comparing high-redshift galaxies to local galaxies, the universe is not static but constantly evolving. In this section I introduce some of the different mechanisms that are driving this evolution.

I first discuss the evolution of star-forming galaxies, and how the correlation between M_* and SFR evolves with z. From this I make some predictions on the star-formation history (SFH) of a Milky-Way–like galaxy. This history implies a sharp difference between the population of high-mass star-forming galaxies at $z \approx 2$, and a precursor of the Milky Way at this redshift. I discuss these different evolutionary paths for galaxies, especially the dichotomy between quiescent
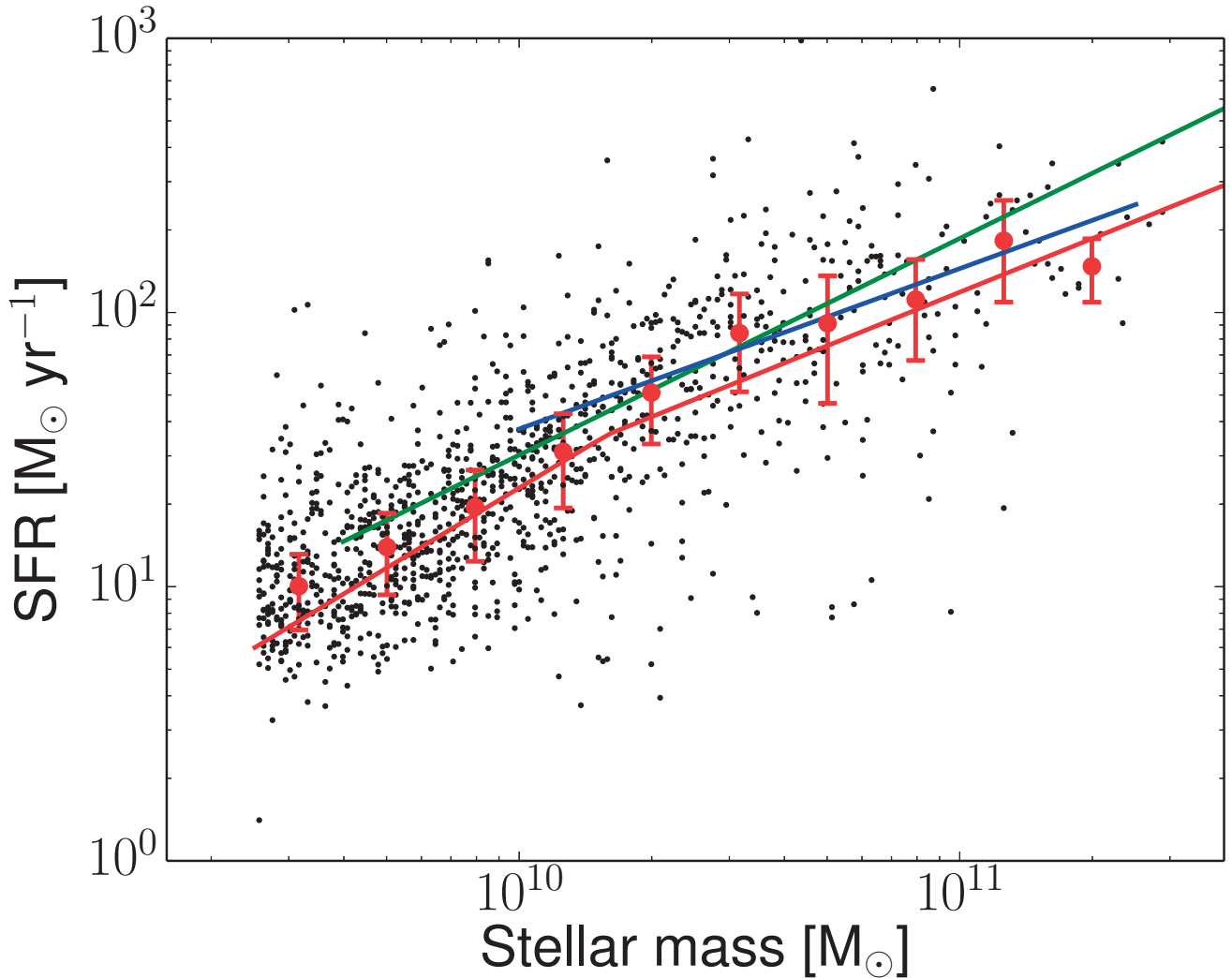
Figure 1.2: SFR as a function of M_* for star-forming galaxies at $z \sim 2$. The black dots indicate star-forming galaxies from the deep-field GOODS-N, with stellar mass estimates from Skelton et al. (2014), and SFR estimates from Whitaker et al. (2014). The red circles indicate the median SFR for the galaxies when binned based on stellar mass. The lines indicate three different parametrizations: red is from Whitaker et al. (2014), green is from Rodighiero et al. (2011), and blue is from Karim et al. (2011).

and star-forming galaxies. And finally I discuss how looking at the structure evolution of galaxies can help us gain insight into these mechanisms.

1.4.1 Evolution of star formation over time

Comparing two galaxies with the same stellar mass, one at high redshift and one in the local universe, the high-redshift galaxy will typically be forming stars at a much higher rate. This can be clearly seen by looking at the star-formation sequence at different redshifts. In Fig. 1.3 we show the stacked measurements from Paper III, showing the typical increase of the SFR towards higher redshift for star-forming galaxies at a fixed M_*. Many measurements exist of the star-formation sequence at different redshifts (e.g. Brinchmann et al. 2004; Noeske et al. 2007; Daddi et al. 2007; Karim et al. 2011; Rodighiero et al. 2011; Bouwens et al. 2012; Whitaker et al. 2014), and the exact shape of the star-formation sequence varies depending on how galaxies are selected, how the SFR is measured and many other factors. One such study was performed by Speagle et al. (2014), which combined data from several surveys calibrating for design differences. Speagle et al. (2014) parametrizes the evolution of the SFR-M_* correlation as a function of the age of the universe (t): $\log \mathrm{SFR}(t) = (\alpha_t t + \alpha_c) \log M_* + (\beta_t t + \beta_c)$, and find a good fit for all included surveys. This fit is in agreement with the stacked measurements from Paper III as seen in Fig. 1.3.

Looking at the Milky Way today, it falls close to the SFR-M_* correlation for star-forming galaxies at $z = 0$. It is interesting to consider how the star-formation history of a Milky-Way–like galaxy (with $M_* \approx 5 \times 10^{10} \, \mathrm{M_\odot}$) would look if this was true for all z. When new stars are formed, stars of different masses are formed following a distribution referred to as the *initial mass function* (IMF). The massive stars will live very short lives, while smaller stars live much longer. As a result of this the distribution of masses for stars will quickly change away from the IMF. Leitner (2012) modelled the evolution of a population of stars, and found that after 100 Myr approximately 45% of the total mass will be lost, either by massive stars dying or through stellar winds from lower mass stars. After the first 100 Myr the evolution is significantly slower. Based on this we model the growth of stellar mass for a galaxy as

$$\frac{dM_*}{dt} = (1 - 0.45) \times \mathrm{SFR}(M_*(t), t) \tag{1.1}$$

where $\mathrm{SFR}(M_*(t), t)$ is the measurement from Speagle et al. (2014). We integrate this backwards in time using a numerical ordinary differential equation (ODE) solver, see Fig. 1.4. In this model the SFR of the Milky-Way–like galaxy peaked approximately 6 billion years ago, which corresponds to $z \approx 1$. The simple model used in this section assumes that the SFR of the mock galaxy is exactly on the star-formation sequence for all z, resulting in a very smooth star-formation history. However, looking at the star-formation sequence the scatter
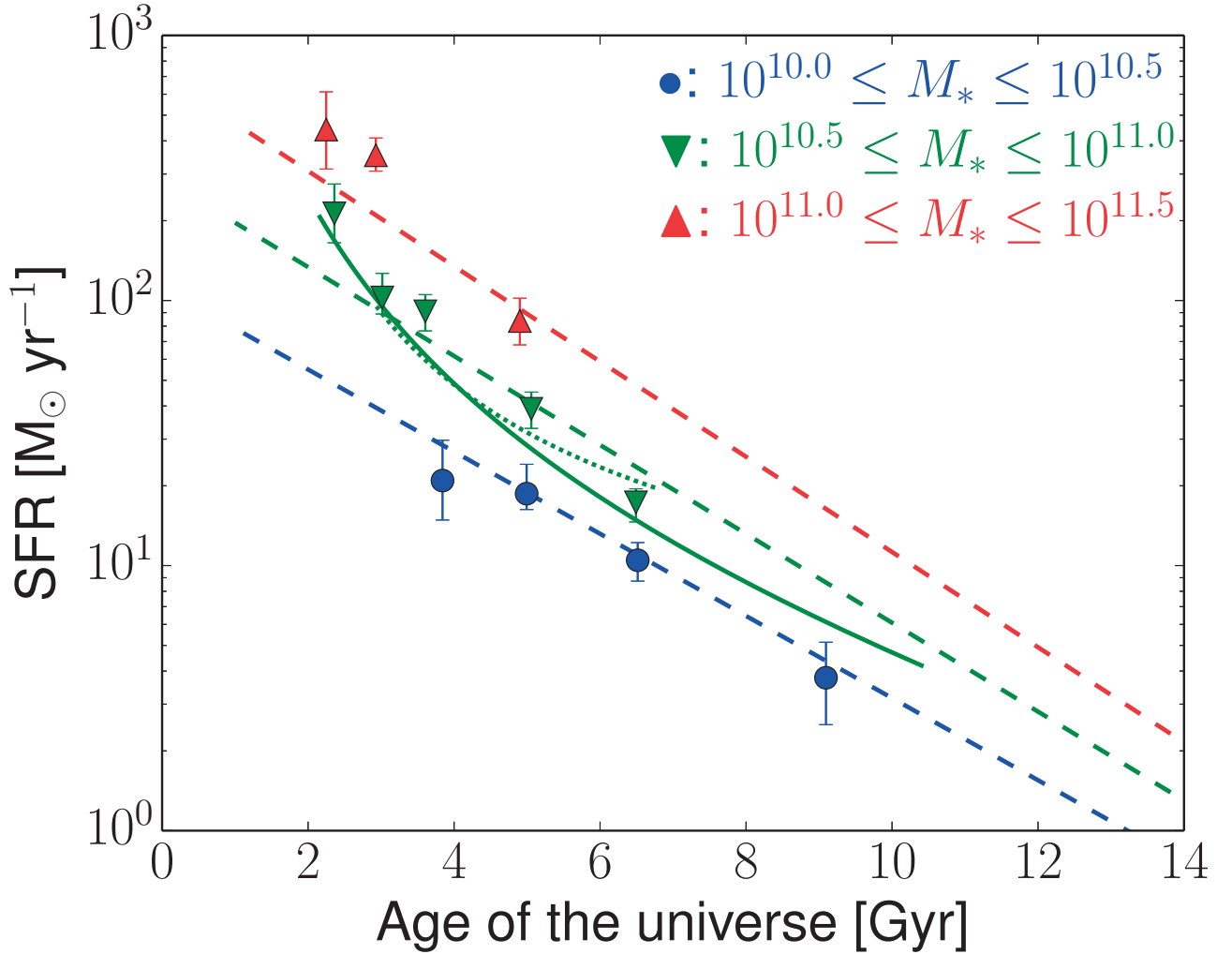
Figure 1.3: SFR on the star-formation sequence as a function of age of the universe. The triangle and circle point are taken from the stacked measurements in Paper III. The full line is the best fit for $M_* = 10^{10.75} M_\odot$ from Karim et al. (2011), the dotted line is the best fit for $M_* = 10^{10.75} M_\odot$ from Whitaker et al. (2014), and the dashed lines are the best fit from Speagle et al. (2014) for $M_* = 10^{10.25}, 10^{10.75}$, and $10^{11.25} M_\odot$.

is large, with galaxies falling below and above. It is possible for galaxies to have highly variable star-formation histories, but still on average fall on the star-formation sequence.

This simple toy model for a Milky-Way–like galaxy gives some insight into the star-formation history of the Milky Way, however, the real picture is more complicated. Observations of stellar populations in the Milky Way indicate that the star-formation history can vary depending on where in the Galaxy we look. However, it is interesting to note that our simple toy model does provide some good agreement with star-formation histories derived from stellar populations in the disk of the Milky Way. E.g., Just & Jahreiß (2010) fit a smooth model to the star-formation history, and their best fit model shows good general agreement with Fig. 1.4. Rocha-Pinto et al. (2000) uses a somewhat different method that look more at variations at shorter time scales, and find evidence for a bursty star-formation history. However, the average shape still agree with 1.4, and Rocha-Pinto et al. (2000) find a large burst at the time where we predict the highest SFR. Such observations are an interesting venue for understanding the evolutionary background of the Milky Way, however, in this thesis the focus is on what can be learned by looking at high-redshift galaxies.

1.4.2   Star formation at $z > 2$

Following the evolution of our Milky-Way–like galaxy according to our simple model back to $z \sim 2.5$, we find that $M_* \approx 10^8$ M$_\odot$. Studies of high-redshift star-forming galaxies rarely study galaxies at such low masses, e.g., Whitaker et al. (2014) is limited to galaxies with $\log \frac{M_*}{\text{M}_\odot} > 8.4$ at $z \sim 1$. The highest-mass star-forming galaxies at $z \approx 2.5$ have $M_* \approx 10^{11.5}$ M$_\odot$. If these galaxies are assumed to evolve following the SFR-M_* correlation for star-forming galaxies, the galaxies would reach $M_* \approx 10^{12}$ M$_\odot$ at $z \approx 0$, approximately 10 times more massive than the most massive disk galaxies in the local universe. Only the most massive cD galaxies have such masses in the local universe, e.g., M87 in the Virgo cluster has $M_* \approx 8 \times 10^{11}$ M$_\odot$ (Murphy et al. 2011). As such, it is clear that most star-forming galaxies must leave the star-formation sequence at some point, dramatically dropping in SFR.

Another way to look at the star-formation history of the universe is measuring the sum of SFR for all galaxies at different redshifts. Doing these measurements, and normalizing to a SFR density using the comoving volume, results in Fig. 1.5. The SFR density peaks at $z \approx 2$ where the Milky Way and precursors of other local disk galaxies are likely to have low stellar masses. The star formation at this time is instead dominated by another class of galaxies, and shows that approximately half of the stars in the current universe were formed before $z \approx 1.0$ (e.g. Marchesini et al. 2009), or within ~ 6 Gyr of the Big Bang. This emphasizes that no universal star-formation history exists for all galaxies.
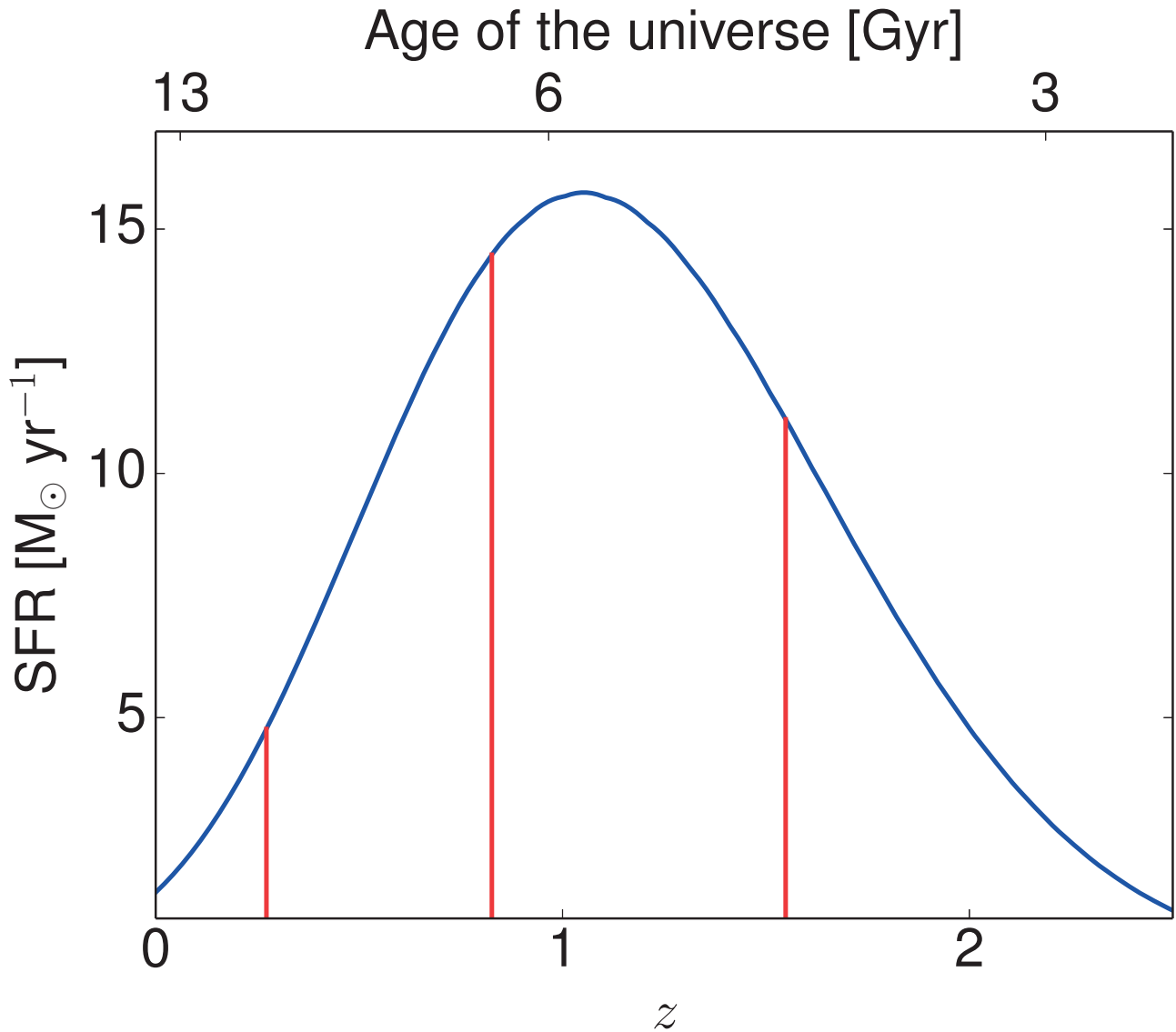
Figure 1.4: SFR as a function of the age of the universe for a Milky-Way–like galaxy ($M_* = 5 \times 10^{10}$ M$_\odot$, assuming that galaxy lies on the SFR-M_* correlation for star-forming galaxies at all z, and that 55 per cent of the stars formed are long-lived. The red lines indicate the times when the galaxy reached 10, 50, and 90% of the current M_*.
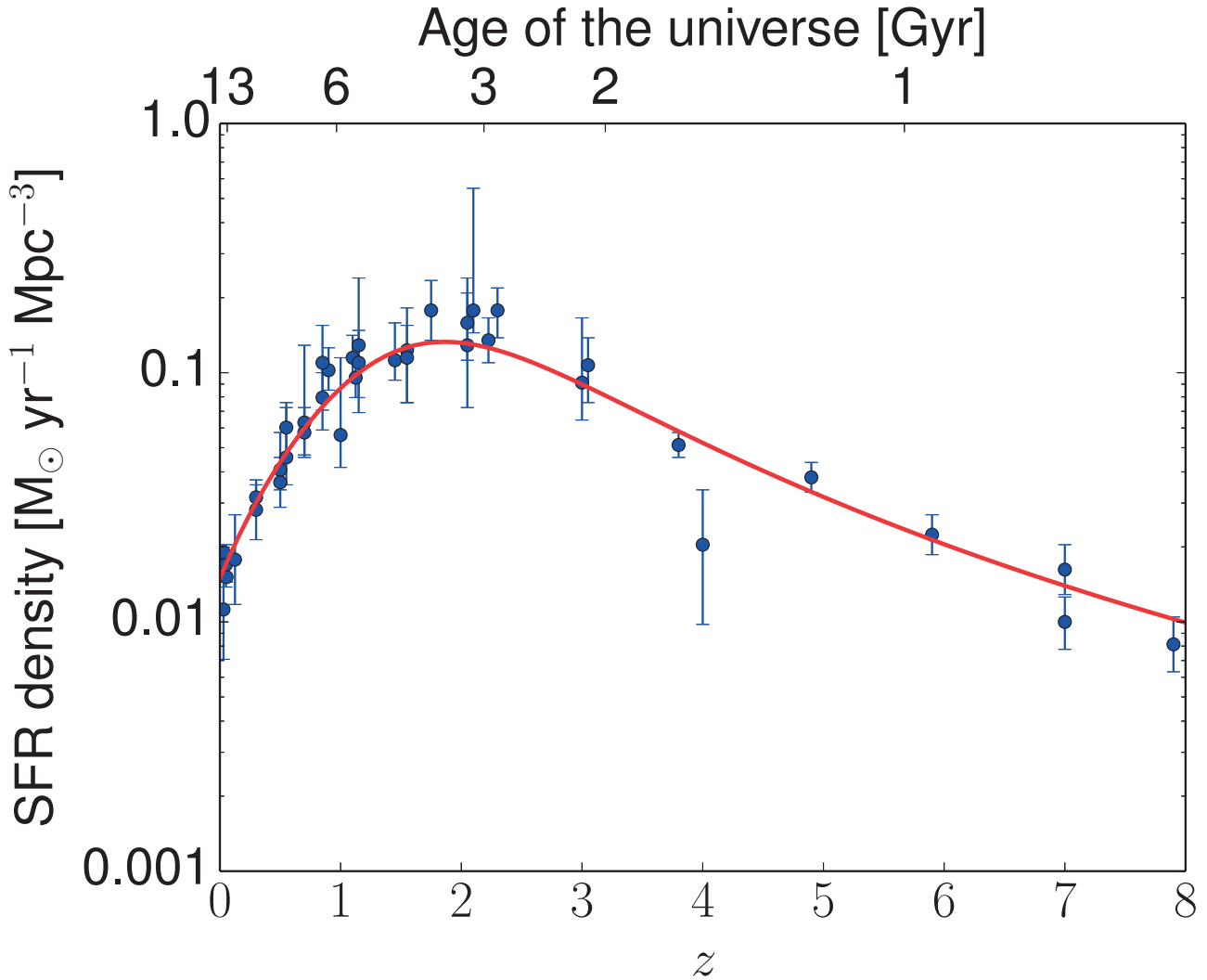
Figure 1.5: SFR density as a function of z. Data assembled by Madau & Dickinson (2014) from Wyder et al. (2005); Schiminovich et al. (2005); Robotham & Driver (2011); Cucciati et al. (2012); Dahlen et al. (2007); Reddy & Steidel (2009); Bouwens et al. (2012); Schenker et al. (2013); Sanders et al. (2003); Takeuchi et al. (2003); Magnelli et al. (2011, 2013); Gruppioni et al. (2013). The red line shows the best fit from Madau & Dickinson (2014) using a double power law, i.e. SFR density $= 0.0015(1+z)^{2.7}\left(1+((1+z)/2.9)^{5.6}\right)^{-1}$.

1.4.3 Connecting star formation to dark matter

What causes some galaxies to form stars earlier than other galaxies? One factor that is important to consider in galaxy formation is dark matter, which makes up $\sim 85\%$ of the mass of the universe (e.g. Planck Collaboration et al. 2014). Stellar masses of galaxies generally follow the masses of the dark matter halos (M_h) (e.g. Behroozi et al. 2013), however, the relation is not linear. At $z = 0$, the ratio M_*/M_h is largest for $M_h \approx 10^{12}\mathrm{M}_\odot$ ($M_* \approx 10^{10}\mathrm{M}_\odot$), with lower ratios for both more massive and less massive dark-matter halos.

Behroozi et al. (2013) studied the evolution of M_* coupled with M_h, and found that the ratio of M_*/M_h peaks for the largest halos at $z > 5$. At lower redshifts the M_*/M_h drops for these halos, indicating that the dark matter halos keep growing while the star formation has decreased. As we move to lower redshift the current day picture takes form, where M_*/M_h peaks for intermediate halo masses. This again supports a picture where SFR decreases when galaxies reach a certain stellar mass.

1.4.4 Quenching

The process that causes the SFR to drop is often referred to as quenching (e.g. Moustakas et al. 2013). Looking at the mass distribution of galaxies in the local universe, quenching happens with M_* in the range $10^{10} - 10^{12}\mathrm{M}_\odot$. It is often modelled as a relatively rapid process (e.g. Moustakas et al. 2013; Speagle et al. 2014). However, this picture is not universally accepted. E.g., Abramson et al. (2016) model the star-formation histories as a smooth function with no rapid cut-off in time for all galaxies, and show that this can reproduce both the star-formation sequence and the bi-modularity seen in observations.

One possible explanation for the quenching is related to the supermassive black holes (SMBHs) in the centre of galaxies. The SMBH masses have been found to correlate with M_* for elliptical galaxies (e.g. Gültekin et al. 2009). Growing SMBHs (active galactic nuclei, AGN) release energy comparable to the binding energy of the whole galaxy (King & Pounds 2015), which can have a profound impact on the galaxy they inhabit. As such there are strong indications that AGN can provide the feedback necessary to quench star formation in massive galaxies (e.g. Fabian 2012). Combined with lower level activity in the AGN, which is common for local quiescent galaxies (Cheung et al. 2016), this can ensure that the SFR remain suppressed until today.

1.4.5 Structure evolution

General reference: Conselice et al. (2014)
In this section I have introduced a broad framework for galaxy evolution, with discussion focused on the integrated properties of galaxies, e.g., SFR, M_*, and

M_h. From this framework it is clear that star formation overall is inefficient, with only 6% of baryonic matter being converted to stars (Fukugita & Peebles 2004), significantly different from predictions from simple theoretical free fall collapse models (Rees & Ostriker 1977). Simulations indicate that effects such as turbulence and feedback from stars could contribute to keeping star formation inefficient (e.g. Goldbaum et al. 2016). Such effects are difficult to study in an integrated sense across the whole galaxy, as they are typically quite local and depend strongly on the location in the galaxy. However, as the resolution and surface brightness sensitivity of observations of high-redshift galaxies improve, it becomes possible to resolve the galaxies.

As discussed in section 1.2, local galaxies are typically classified based on Hubble type. Looking at the evolution at $z < 1$, the evolution largely mirror that of star-forming versus quiescent galaxies, where spiral galaxies are becoming less common and elliptical galaxies more common. However, an even more significant difference is found in the number of peculiar galaxies, i.e., irregular galaxies and ongoing mergers. Buitrago et al. (2013) classified galaxies based on visual inspection, and found at $z \approx 0$ only 3% of the galaxies are peculiar, while at $z > 1$ peculiar galaxies are equally common to late type galaxies. This emphasises the differences in star formation at high redshifts, and indicates that Hubble classification may not be the most useful tool to study structure evolution. Again, note that while there is a similar dichotomy for the Hubble classifications, and the star-forming versus quiescent classification, there is no one-to-one mapping between the two classes.

Another parameter that has garnered some interest is the evolution of the sizes of galaxies, especially with the discovery of a class of very compact quiescent galaxies at high redshift (e.g. Daddi et al. 2005). It is seen for all classes of galaxies that sizes grow smaller at high redshift, however, the effect is strongest for quiescent galaxies. van der Wel et al. (2014) parametrized the size evolution for star forming and quiescent galaxies with $M_* \approx 5 \times 10^{10} M_\odot$, using $r \propto (z + 1)^\beta$. They found $\beta \approx -1.48$ for quiescent galaxies, and $\beta \approx -0.76$ for star-forming galaxies. The rapid evolution of sizes for quiescent galaxies is often thought to be driven by minor mergers (e.g. Carrasco et al. 2010), but star-forming galaxies being quenched and moving into the quiescent category also contribute to change the size distribution.

The size evolution for star-forming galaxies is less clear. Mo et al. (1998) predict that if galaxies are supported by rotation, the size should evolve as if $\beta \approx -1.5$, this is clearly not the case for star-forming galaxies. van der Wel et al. (2014) point out that the scaling of the sizes of galaxies is similar to the scaling of the size of the dark matter halos, however, it is not clear why this is the case. In the inside-out scenario, the size growth of the galaxy is driven by formation of new stars in the outer regions. There is some support for this model looking at the ages of stars at different radii in local disk galaxies (e.g. Dale et al. 2016). One

Table 1.1: Some common photometric filters

Name	Central wavelength
U	370 nm
B	450 nm
V	550 nm
R	660 nm
I	810 nm
z	900 nm
Y	1.0 μm
J	1.2 μm
K	1.6 μm
L	2.2 μm
IRAC 1	3.6 μm
IRAC 2	4.5 μm
IRAC 3	5.8 μm
IRAC 4	8.0 μm

method that can be used to determine the importance of new star formation as a driver of size evolution, is mapping high-redshift galaxies in submillimetre (submm) and radio wavelengths. Emission from galaxies at these wavelengths is primarily from young and newly formed stars (see section 1.7), and in chapter 4 we will discuss some conclusion based on such measurements.

1.5   Colour selection criteria

An important aspect of the study of high-redshift galaxies is finding and selecting galaxies. This section discusses some different techniques used to identify galaxies.

Searching for high-redshift galaxies is often done using imaging photometry. This allows to maximise the amount of sky covered for a given depth. Observations use a number of different filters. Once sources are identified using one or multiple filters, flux densities of sources are measured in all filters using an aperature centred on the coordinates of the sources. In Table 1.1 we list some commonly used photometric bands. Similar band designations exist at radio wavelengths, e.g., L band can refer to observations at 1.4 GHz. However, in this work band designations will only be used to refer to optical and infrared bands, and radio observations will be specified in terms of frequency or wavelength.

Selection criteria can be defined using the measured flux densities in different photometric bands. The trick is to define criteria, that based on a typical spectral energy distribution (SED) of a galaxy, will only select galaxies of a desired type. Fig. 1.6 illustrates the SEDs for three typical star-forming galaxies at
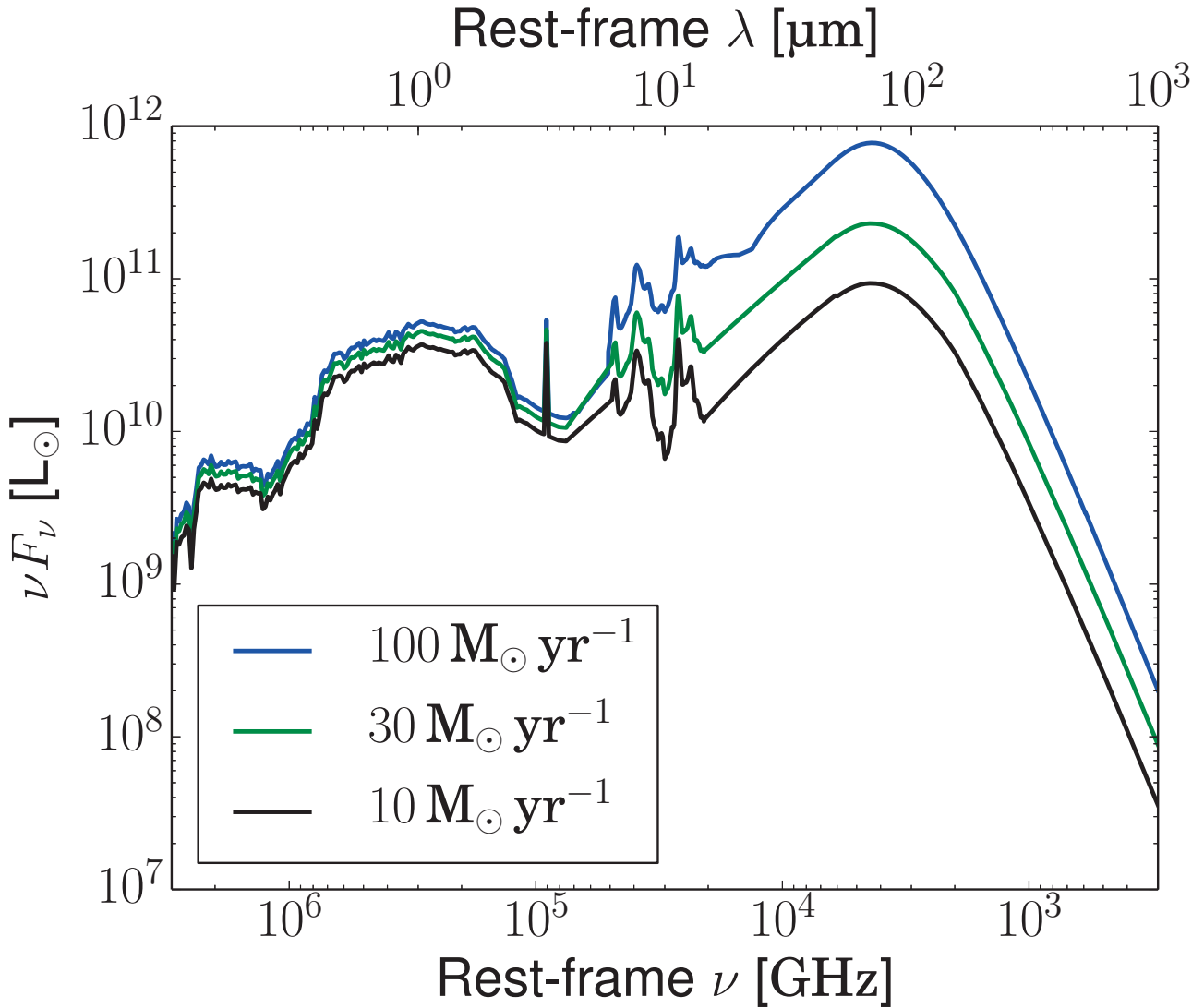
Figure 1.6: Typical spectral energy distribution (SED), from rest frame ultraviolet to far-infrared, for star-forming galaxies at redshift $z = 3$ (Chary & Elbaz 2001).

$z \approx 3$. This SED can be divided roughly into two bumps, one bump at shorter wavelength, in rest frame peaking in visible light, and is dominated by light coming directly from the stars. The other bump, at longer wavelengths dominated by thermal emission from interstellar dust heated by the stars. These two bumps are roughly equal in total energy emitted. Light is also emitted at shorter and longer wavelengths, but this is a small contribution to the energy budget compared to the visible and infrared features.

1.5.1 Extremely Red Objects

A natural method to select distant galaxies is looking for red objects. The more distant a galaxy is, the more redshifted it will be. Elston et al. (1988) showed

that it was possible to find high redshift galaxies with

$$\frac{F_K}{F_R} > 21.88 \tag{1.2}$$

where F_K and F_R are the flux densities measured in the K and R filters. These galaxies are refered to as Extremely Red Objects (EROs). It is common to work with flux densities from galaxies in terms of magnitudes, and in AB magnitudes the criterion becomes $R - K > 3.7$. Note, that redshift is not the only reason that a galaxy may be red. Quiescent galaxies, as well as galaxies with large amounts of dust, will be intrinsically redder compared to typical star-forming galaxies. As such the criterion will tend to select galaxies of these types.

1.5.2 Lyman-break galaxies

One of the strongest features in the SED of star-forming galaxies, is the *Lyman break*. The Lyman break is located at 912 Å, where all photons with higher energy can ionize neutral hydrogen (e.g. Leitherer & Heckman 1995). This causes the flux density to drop drastically for wavelengths shorter than 912 Å. It is possible to design a criteria around this break to select galaxies at a specific redshift range. For galaxies around $z \approx 4$ the photometric bands U, G and R (365, 600 and 660 nm) can be used. In this case the Lyman break falls between the U and G band, leading to low flux in U, and approximately flat spectrum between G and R. The original criteria used by Steidel et al. (1995) were

$$\frac{F_G}{F_U} > \left(\frac{F_R}{F_G}\right)^4 \tag{1.3}$$

and

$$\frac{F_R}{F_G} > 3.02 \tag{1.4}$$

where F_G, F_R and F_U are the flux density in the U, G and R band. Typically the Lyman-break criteria are expressed in term of magnitude differences instead of flux density ratios. In AB magnitudes these criteria become $U - G > 4(G - R)$ and $G - R > 2.76$. A galaxy that satisfies the Lyman-break criteria is referred to as a *Lyman-break galaxy* (LBG). The exact bands used are often shifted around a little depending on the data available in different surveys. This will change the exact criteria but the general principle is the same. Equivalent criteria can be used to detect galaxies at higher redshift by shifting all used bands to longer wavelengths (Steidel et al. 1999). This has been used to search for galaxies as far out as $z \approx 10$, e.g., Bouwens et al. (2011).

The Lyman-break criteria work well for galaxies with intrinsically blue colours, which results in a strong break in the SED. If a galaxy is very dusty, or has no young stars, the LBG criteria will not work well.

1.5.3   BzK galaxies

Another strong feature in the SED of a typical galaxy is the break at $\sim$400 nm, often referred to as the *4000Å break*. Nearby this break, at $\sim$360 nm, there is also the *Balmer break*, that results from the hydrogen Balmer series. The longer wavelength of these two breaks, compared to the Lyman break, makes them significantly less dependant on the intrinsic colour of galaxies. Older and less massive stars are still very bright at $\sim$400 nm and dust obscuration will be less significant. Using this fact, Daddi et al. (2004) defined the BzK criteria. The BzK criteria are named after the three photometric bands used in the selection: B, z, and K. These criteria selects to galaxies around $z \approx 2$. By tweaking the selection criteria, we can also determine if the galaxy is star forming or more quiescent.

The BzK criterion for star-forming galaxies is

$$\frac{F_K}{F_z} > 1.2\frac{F_z}{F_B} \tag{1.5}$$

or $(z - K) - (B - z) > -0.2$ in AB magnitudes. For quiescent galaxies the criteria instead become

$$\frac{F_K}{F_z} < 1.2\frac{F_z}{F_B} \tag{1.6}$$

combined with

$$\frac{F_K}{F_z} > 10 \tag{1.7}$$

or $(z - K) - (B - z) < -0.2 \cap (z - K) > 2.5$ in AB magnitudes. Star-forming galaxies selected with the BzK criteria are referred to as sBzK galaxies or sBzKs, while quiescent galaxies are referred to as passive BzK galaxies or pBzKs.

1.5.4 UVJ selection

Large photometric surveys can contain a large number of photometric bands, not only two or three bands as used by the criteria defined so far in this section, e.g., Skelton et al. (2014) catalogue has data from ~ 25 different photometric filters. An approach that has become more common for such catalogue, is to fit a SED template to the flux densities in the different bands. This allows identifying the redshift of all objects in the catalogue, resulting in so-called *photometric redshift*. Photometric redshifts are not as accurate as spectroscopic redshifts (e.g. Hildebrandt et al. 2010; Dahlen et al. 2013; Wittman et al. 2016), however, photometric redshifts are significantly easier to obtain for large samples of galaxies.
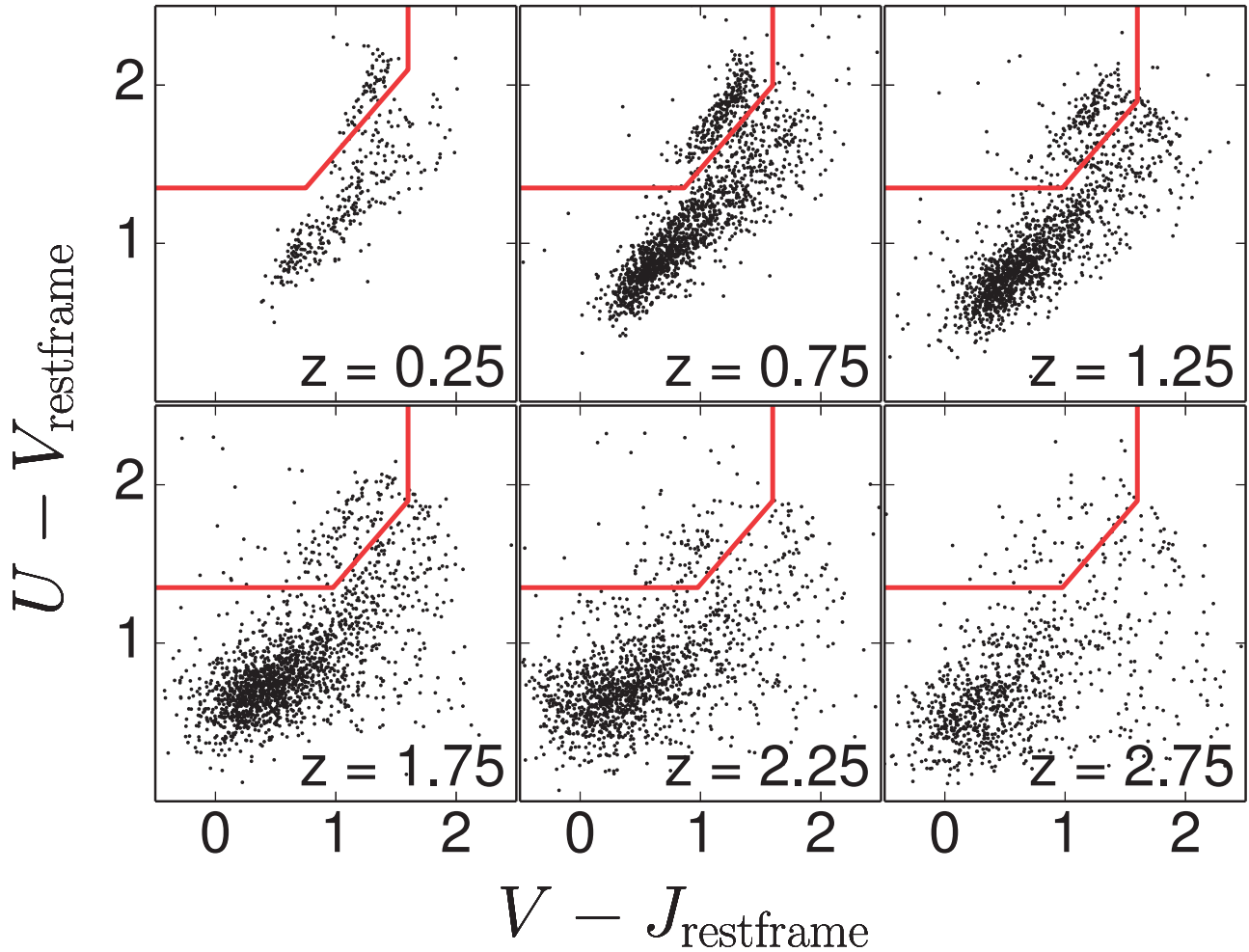
Figure 1.7: Galaxies from the Skelton et al. (2014) catalogue, split by redshift in bins with a width of 0.5. The red lines indicate the selection criteria from Williams et al. (2009).

The UVJ criteria are defined to separate star-forming and quiescent galaxies in a sample where the photometric redshifts are known. Using the photometric redshifts, the rest frame flux densities in the U, V, and J band are calculated from flux densities in the measured bands. Quiescent galaxies have been found to follow a significantly different track in the $U - V$ vs. $V - J$ plane Williams et al. (2009). In Fig. 1.7 is shown the $U - V$ vs. $V - J$ for a number of galaxies in different redshift bins with data from Skelton et al. (2014). The galaxies in the top left, surrounded by red lines, are selected as quiescent galaxies.

1.5.5   Distant Red Galaxies

Another criterion sometimes used is

$$\frac{F_K}{F_J} > 3.37 \tag{1.8}$$

where F_K and F_J are the flux densities in K and J band, (Franx et al. 2003, $J_{AB} - K_{AB} > 1.32$ in AB magnitudes) .

This criterion also select galaxies based on the Balmer/4000Å break, and galaxies selected with it are referred to as Distant Red Galaxies (DRGs). The criterion has been found to select massive galaxies around redshift 2. The selection of red galaxies may include those with old stellar populations that are relatively deficient in blue light, as well as galaxies with a large content of dust that obscures the light from young stars.

1.6   Brightness profiles of galaxies

When measuring the sizes of galaxies, it is important to consider how the size is defined. In this section I will discuss two common definitions, the Sérsic effective radius (R_e) and the Gaussian full-width at half-maximum (FWHM). These two definitions are based on brightness profiles of the galaxies, i.e., how the surface brightness depends on distance from the centre of the galaxy. de Vaucouleurs (1948) found that the brightness profiles of elliptical galaxies could be well modeled using

$$I(R) = I_e e^{-7.669\left[\left(\frac{R}{R_e}\right)^{\frac{1}{4}} - 1\right]} \tag{1.9}$$

where I_e is the surface brightness at R_e, and R_e is the effective radius, i.e., the radius that encloses 50% of the total flux density. This relations is referred to as de Vaucouleurs' law. To allow fitting of larger sets of galaxies Sersic (1968) created a more generalized profile, referred to as the Sérsic profile:

$$I(R) = I_e \exp\left\{-b_n\left[\left(\frac{R}{R_e}\right)^{\frac{1}{n}} - 1\right]\right\} \tag{1.10}$$

where n is the Sérsic index and b_n is a normalization factor. The factor b_n can be found by solving

$$\int_0^{b_n} e^{-t} t^{2n-1} dt = 0.5 \int_0^{\infty} e^{-t} t^{2n-1} dt. \tag{1.11}$$

A good approximation of b_n is

$$b_n = 1.9992n - 0.3271 \tag{1.12}$$

for $1 \leq n \leq 4$.

Using the Sérsic profile, most elliptical galaxies can be well fitted with $n \approx 4$ (e.g. Blakeslee et al. 2006). For spiral galaxies the brightness profile is generally not as smooth. Blakeslee et al. (2006) has shown that for smoother spiral galaxies, the brightness profile can be well fitted with $n \approx 1$, but for galaxies with more irregular structure the best fit n is often larger. As such the Sérsic index in combination with a measure of the smoothness of the surface brightness can be used to classify galaxies with high accuracy. More important for the size measurement is a consistent treatment.

At radio and submm wavelength another profile, the Gaussian profile, is commonly used (e.g. Simpson et al. 2015; Ikarashi et al. 2015). The profile is defined as

$$I(R) = \frac{\Phi}{2\pi\sigma^2} \exp\left(-\frac{R^2}{2\sigma^2}\right) \tag{1.13}$$

where Φ is the flux density and σ is the size. The size is often defined in terms of the FWHM instead: $\text{FWHM} = 2\sqrt{2\ln 2}\sigma \approx 2.35\sigma$. Note that the Gaussian profile is equivalent to a Sérsic profile with $n = \frac{1}{2}$ and $R_e = \sqrt{2\ln 2}\sigma$. In Paper III we compare sizes derived from the Sérsic and Gaussian profile for marginally resolved galaxies, and find that the effective radii are typically similar.

1.7 Longer wavelength observations of distant galaxies

A large focus in this thesis is on what can be learned about galaxy evolution from observations at longer wavelengths. While most galaxies can be found using surveys in visible light and near-infrared, a more complete picture is obtained by looking at more of the electromagnetic spectrum. Moving from the near-infrared into the mid- and far-infrared, we can observe the dust emission from galaxies. The dust is primarily heated by hot young stars and as such this emission can be used to trace ongoing star formation.

However, Earth's atmosphere is opaque over a large part of the infrared range, and consequently it is very difficult to observe galaxies near the peak of the far-infrared dust SED. Observations at these wavelengths require space based telescope, e.g. *Herschel Space Observatory*. The cost and technical challenges of launching a telescope into space limits the size of space based telescopes. Due to diffraction the size, or more specifically the diameter of the aperture (D), limits the resolution of a telescope according to $\Theta \approx 1.22\frac{\lambda}{D}$ where Θ is typical angular resolution and λ is the wavelength of the observations. For *Herschel Space Observatory* the angular resolution is $\sim 20''$ at 300μm.[5] This makes it challenging to study faint galaxies, as they will be blended with emission from other sources within the large beam.

---

[5] $20''$ corresponds to $\sim$170 kpc at $z \approx 2$

1.7.1   Submm dust continuum

An option to study the dust emission is to go to mm wavelengths. When the wavelength approaches a little less than one mm, the atmosphere is transparent enough to observe from the top of high mountains, at sites such as Chajnantor plateau in Chile or Mauna Kea in Hawai'i. At these wavelengths we are still sensitive to the dust emission. By combining a large number of dishes into an interferometer we can also achieve good resolution at these wavelengths. The most sensitive interferometer at mm wavelengths is the Atacama Large Millimeter/sub-millimeter Array (ALMA), with an angular resolution $< 1''$ across the covered wavelength range.

An advantage with observing at these wavelengths is that the redshift does not strongly impact the expected flux density. The higher the redshift of the target galaxy, the closer to the dust emission peak we will observe it. This results in the so called *negative K-correction*, where, for a given far-infrared luminosity, the observed flux is almost constant for redshift $z = 1 - 8$.

The dust emission can often be described approximately as a modified black body (e.g. Beelen et al. 2006)

$$F_\nu \propto \nu^\beta B_\nu(T_{\text{dust}}) \tag{1.14}$$

where $B_\nu(T_{\text{dust}})$ is the Planck function and T_{dust} is the dust temperature. From this we calculate the IR luminosity of the galaxy (L_{IR}) as the integral of the total modified black body emission from 8 µm to 1000 µm.

To calculate L_{IR} from our data we need to account for the redshift of our target source. If we measure a source $z = 2$ using ALMA, with the band 7 receiver ($\nu \approx 345\,\text{GHz}$), we are in fact sampling the dust SED at $(z+1)\nu \approx 1.035\,\text{THz}$. We also must consider that the ALMA bands will cover a larger part of the SED. To correct for this the measured flux must be divided by $(z+1)$.

Finally, we need to go from flux density to total luminosity. This involves using a cosmological model, in this thesis a flat universe with $\Omega_M = 0.315$ and $H_0 = 67.3\,\text{km s}^{-1}\,\text{Mpc}^{-1}$ (Planck Collaboration et al. 2014) is assumed. Using this we can calculate the luminosity distance $D_L(z)$.

Combining all we arrive at

$$L_{\text{IR}} = 4\pi D_L^2(z) \int_{c/1000\,\mu m}^{c/8\,\mu m} \nu^\beta B_\nu(T_{\text{dust}}) \frac{F_{\nu_{\text{obs}}}}{((z+1)\nu_{\text{obs}})^\beta B_{(z+1)\nu_{\text{obs}}}(T_{\text{dust}})} d\nu \tag{1.15}$$

where ν_{obs} is the frequency of the observations. We then convert this into a star formation rate

$$\frac{\text{SFR}_{\text{FIR}}}{\text{M}_\odot\,\text{yr}^{-1}} = 1.3 \times 10^{-10} \frac{L_{\text{IR}}}{L_\odot}. \tag{1.16}$$

This is the same conversion used in Paper II and is based on the calibration by Kennicutt (1998) adapted with a Chabrier (2003) initial mass function. The

shape of the IMF is important for star formation measures, as it determines the number of massive stars that are formed for a given star formation rate.

1.7.2 Radio continuum

Another method to measure the star formation of galaxies is to go to even longer wavelengths. Stars with masses greater than around eight solar masses will go supernovae after a few tens of million years. Such supernovae will eject large number of relativistic electrons that will lead to synchrotron radiation. This means that a galaxy with recent star formation will emit light at wavelengths around a few tens of cm, this emission has been shown to be an effective measure of star formation (Condon 1992). Unlike measures of star formation using ultraviolet or infrared radiation, radio continuum is independent of dust extinction. However, if the galaxy contains an active galactic nuclei (AGN), this may also emit light at similar wavelengths. As such it provides a valuable independent measure of the SFR of galaxies with low AGN activity. There are several interferometers operating at radio wavelengths, the most sensitive is the Karl G. Jansky Very Large Array (VLA).

For radio continuum we convert the flux into a luminosity in a similar manner assuming that the SED in radio follows a power law

$$F_\nu \propto \nu^\alpha. \tag{1.17}$$

This results in a radio luminosity of

$$L_\nu = \frac{4\pi D_L^2(z)}{(1+z)^{1+\alpha}} F_\nu \tag{1.18}$$

where F_ν is the measured flux at observer-frame frequency ν and L_ν is corrected to be the luminosity at rest-frame frequency ν. Using the model from Condon (1992) adapted to a Chabrier (2003) we convert this into a SFR

$$\frac{\mathrm{SFR}_{1.4\,\mathrm{GHz}}}{\mathrm{M_\odot\,yr^{-1}}} = 3.18 \times 10^{-22} \frac{1.4\,\mathrm{GHz}}{\mathrm{W\,Hz^{-1}}} \tag{1.19}$$

The spectral index α has been found to be around -0.8 and we use this value.

1.7.3 Expected flux densities of high-redshift galaxies

Fig. 1.8 shows a few examples of spectral energy distributions (SED) for high-redshift, star-forming galaxies. For comparison we include the sensitivity of ALMA and VLA, currently the most sensitive interferometers at their respective wavelengths. At $z = 3$, it is difficult to observe galaxies with star formation rates below a few tens of solar masses per year. A technique that can be used
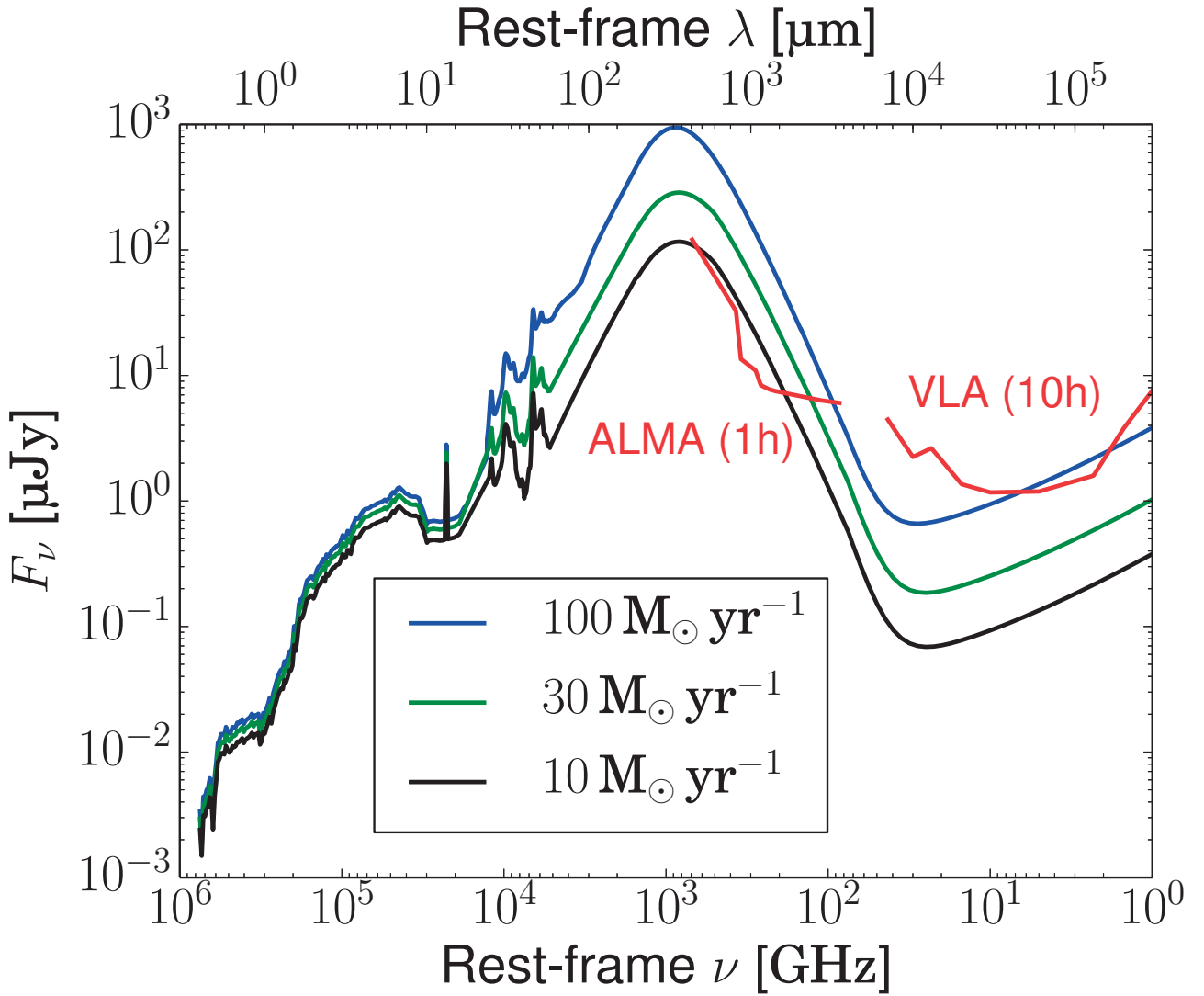
Figure 1.8: SED of three star-forming galaxies at $z = 3$. Red curves indicate the sensitivity of full ALMA and VLA, respectively. Note that in contrast to Fig. 1.6 we plot F_ν not νF_ν, however it is the same SED extended to longer wavelengths.

to be push past this is *stacking*. Stacking is a statistical method that can be used to obtain the average properties of populations of galaxies. ALMA is an extremely sensitive telscope and, with the negative K-correction, it is efficient to detect star-forming galaxies at high-redshift. However, the field of view (FOV) is small ($\sim$0.1 arcmin^2 at 345 GHz), making it difficult to study large samples of galaxies. Large fields can be studied using mosaics, where the observation time is divided across many different pointings. Such observations will not be as deep as observations of individual galaxies can be, but using stacking we can accurately estimate the average properties of galaxies that would otherwise fall below the sensistivity limit. VLA is not as sensitive to star-forming galaxies as ALMA, however, VLA has one advantage over ALMA: the field of view is significantly larger. A single observation of VLA at 1.4 GHz can cover ~ 0.3 square degrees, which can observe 1000s of star-forming galaxies at once. In this context stacking is again extremely powerful, as individual detections for many of these galaxies would be beyond even the longest integrations with VLA.

Stacking

Stacking is a statistical method to measure the average properties of sources that are too faint to be detected directly. It relies on *a priori* information on the location of the target sources. It works by averaging the emission from all target sources, and will result in a noise $\frac{\sigma}{\sqrt{N_{\text{stack}}}}$ where σ is the typical noise without stacking and N_{stack} is the number of target sources. Fig. 2.1 illustrates a simple stacking procedure. A sample of sources is selected, i.e., a list of positions where we expect faint emission. For each position a 64×64 pixel stamp is cut out of the full image. All stamps are then averaged together on a pixel-by-pixel basis. This results in a stacked image with significantly lower noise than the individual stamps.

The technique of stacking is especially useful for studying the submm and radio emission of high-redshift galaxies. Using the large photometric catalogues from near ultraviolet to near infrared, such as MUSYC (Gawiser et al. 2006; Quadri et al. 2007; Cardamone et al. 2010) and the COSMOS catalogue (Capak et al. 2007), we can identify large samples of high-redshift galaxies. These galaxies can then be stacked in submm and radio maps, which will allow us to study galaxies that would otherwise be out of reach of these telescopes.

For observations with single-dish telescopes at submm and radio wavelengths the angular resolution is limited from around 20″ at 345 GHz to around 10′ at 1.4 GHz . This is significantly larger than the typical size of a high-redshift galaxy, which is typically less than 1″ (e.g. Toft et al. 2007). This makes it difficult to ensure that the stacked emission originates from the target galaxies, and risks blending the emission from multiple galaxies in our beam. To avoid these issues we can use interferometric telescopes, such as ALMA and VLA, which have much higher angular resolution. However, for interferometry, stacking is complicated by the fact that interferometry is not a direct imaging method. We are required to model the data to produce an image of the source. In Paper I we investigate stacking of interferometric data, in particular for VLA and ALMA.
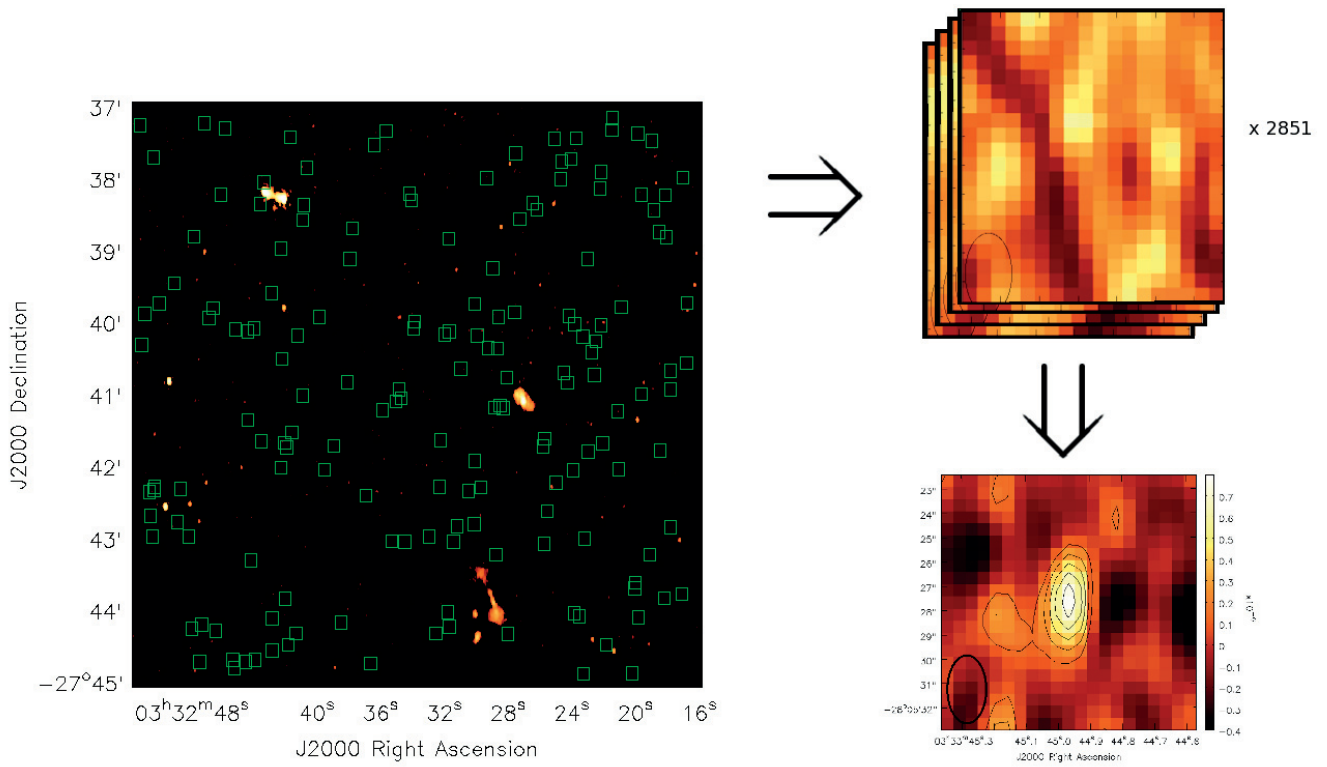
Figure 2.1: Illustration of stacking in the Extended Chandra Deep Field-South (ECDFS). In the example ∼3000 Lyman-break galaxies are stacked in the Miller 1.4 GHz VLA map of the ECDFS (Miller et al. 2013). (Left) A $10'\times10'$ segment of the 1.4 GHz VLA map. The stacking positions are marked in the map with green squares. (Top right) Map in a 16×16 pixel region around a typical stacking position, showing no detection. (Bottom left) Stacked image, showing 5σ detection.

We propose a new method to perform stacking, where the stacking is performed in the uv-domain.

In this chapter I will first give an introduction to interferometry (section 2.1). In section 2.4.1 I expand on the discussion of the simulations used in the Paper I.

2.1 Interferometry

Interferometry aims to simulate a large telescope by a collection of smaller telescopes. By using a technique known as *aperture synthesis*, we can produce an image with a typical resolution element of $1.22\lambda/D$, where D is the largest separation of dishes. This technique was originally developed by Martin Ryle and colleagues.

During observations each antenna records the incoming power over time to each antenna j as $P_j(t)$. A *visibility* is calculated between a pair of antennas j and k as

$$V_{j,k}(T) = \int_T^{T+\Delta T} P_j(t)P_k(t)dt + i \times \int_T^{T+\Delta T} P_j(t)P_k(t+0.25/\nu)dt, \qquad (2.1)$$

where i is the imaginary unit, T is the observation time, ΔT is the integration time, and ν is the frequency. This quantity is connected to the source we want to observe as

$$V_{j,k}(T) = \int_{\text{sky}} A_N(\vec{\sigma})I(\vec{\sigma})e^{-\frac{2\pi i}{\lambda}\vec{B}_{j,k}\cdot\vec{\sigma}}d\Omega, \qquad (2.2)$$

where $\vec{\sigma}$ is a unit vector pointing towards the position on the sky, $A_N(\vec{\sigma})$ is the primary beam attenuation, $I(\vec{\sigma})$ is the source brightness, and $\vec{B}_{j,k}$ is the separation of antenna j and k at the time T.

The position vector $\vec{\sigma}$ is generally expressed in terms of a local rectilinear coordinate system (l,m) where l is in the east direction and m is in the north direction. The origin in this coordinate system is called the *phase centre*.

The primary beam attenuation depends on the antenna properties, such as size, location of the sub reflector, etc. In this work we assume that all antennas within the array are similar, as is true for VLA and the ALMA main array. For telescopes with parabolic main reflector dishes, such as the VLA and ALMA antennas, we can approximate the primary beam attenuation as

$$A(l,m) = e^{-\frac{2\ln 2(l^2+m^2)}{(1.22\lambda/D_{\text{dish}})^2}}, \qquad (2.3)$$

where D_{dish} is the antenna dish diameter and where it is assumed that the antennas are pointing towards the phase centre.

2.1.1 uv-**coverage**

The separation between antennas $\vec{B}_{j,k}$ is often expressed in terms of (u, v) that are defined such that $\vec{B}_{j,k} \cdot \vec{\sigma} = \lambda(ul + vm)$, i.e., (u, v) is the separation of the antennas in wavelengths as seen looking down from the phase centre. This simplifies equation 2.2 to

$$V(u, v) = \int_{\text{sky}} A_N(l, m) I(l, m) e^{2\pi i (ul + vm)} \, dl \, dm, \qquad (2.4)$$

or the 2D Fourier transform of $A_N(l, m) I(l, m)$ evaluated at (u, v). The 2D Fourier transform can be inverted to

$$I(l, m) = \frac{1}{A_N(l, m)} \int V(u, v) e^{-2\pi i (ul + vm)} \, du \, dv. \qquad (2.5)$$

The plane spanned by (l, m) is referred to as the *image-plane* and the plane spanned by (u, v) is referred to as the *uv-plane*. We can only sample $V(u, v)$ where we have a pair of antennas with separation (u, v). The points in the uv-plane where we have sampled $V(u, v)$ are referred to as the *uv-coverage*. Fig. 2.2 illustrates the uv-coverage for a typical configuration of VLA. In each integration we sample two points for each possible pair of antennas, i.e., in total, $N_{\text{antennas}}(N_{\text{antennas}} - 1)$ points are sampled where N_{antennas} is the number of antennas. As Earth rotates each pair traces out a track in the uv-plane, leading to greater uv-coverage.

As seen in figure 2.2 there is a "hole" in the middle of the uv-plane with no sampling. This "hole" is set by the closest antennas in the array. For sources with large spatial extent flux will be lost, since most of this will fall inside the "hole". Similarly we cannot sample $V(u, v)$ outside the largest separation of antennas. This limits our resolution. However, for sources with small spatial extent, the full flux can still be sampled on shorter baselines. These effects can also be understood as a band-pass filter on the imaged data, where components with spatial scales outside the uv-coverage are filtered.

2.1.2 Imaging

The most common method used to find $I(l, m)$ is the Fast Fourier Transform (FFT). This requires $V(u, v)$ to be sampled at regular intervals, which the uv-coverage is not. To fix this *uv-griding* is performed. This divides the uv-plane into a N×N grid. For each grid point the value is calculated from the visibilities that fall within the grid element. However, the uneven sampling of the uv-plane leads to very different number of visibilities in each grid point. Some grid positions contain no visibilities at all. From this we can define a sampling S, a N×N grid with the number of visibilities in each grid point. Running FFT
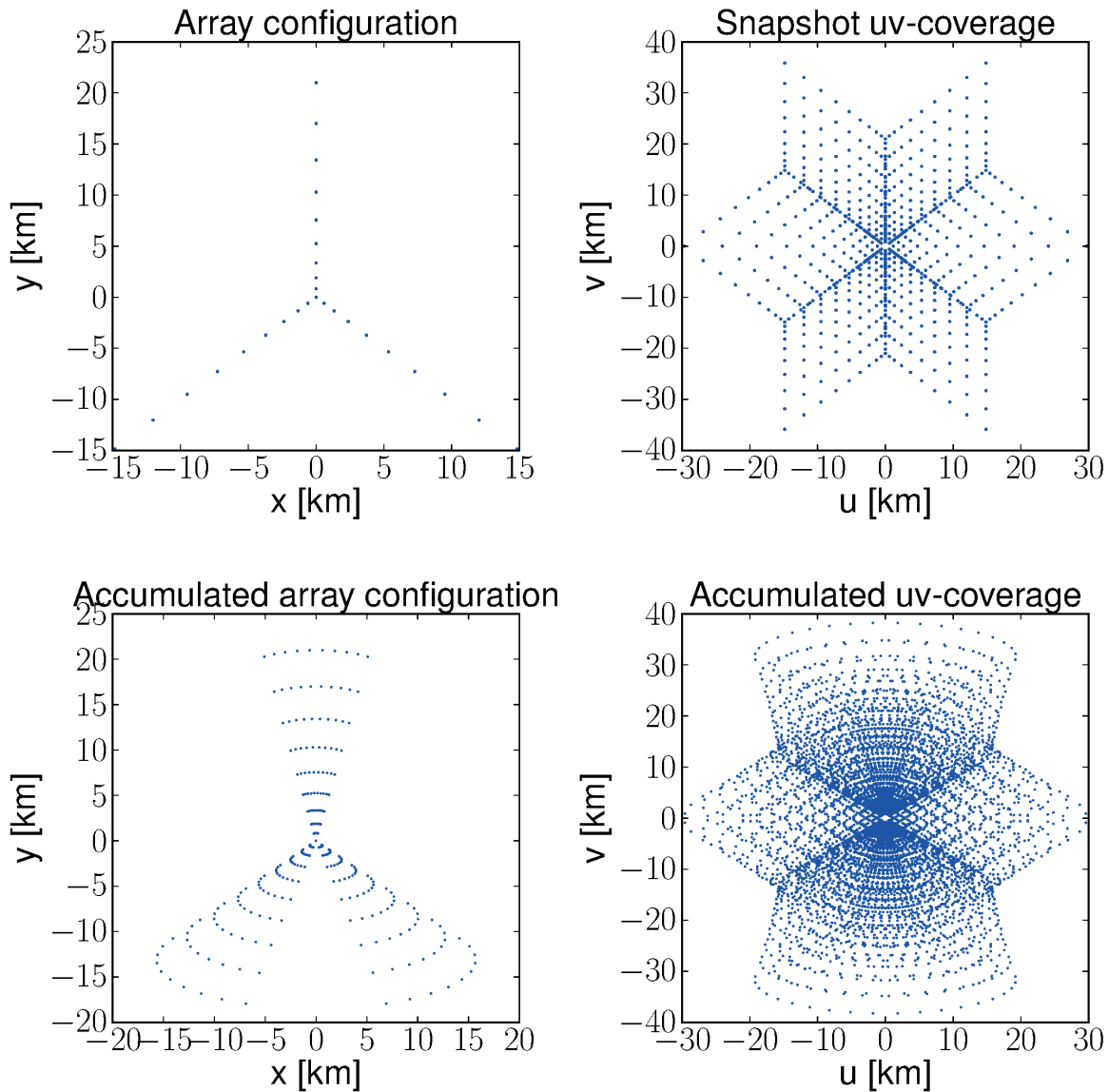
Figure 2.2: Illustration of array configuration and *uv*-coverage of VLA. Observation at a declination of 10° with a configuration similar to the VLA A configuration. (Top left) The VLA array configuration as seen from the source. (Top right) The corresponding *uv*-coverage to the VLA array configuration. (Bottom left) As Earth rotates, the array as seen from the source changes. The image shows how the array changes from 3 hours before the source passes the meridian until 3 hours after. (Bottom right) We accumulate the snapshot *uv*-coverages to cover the *uv*-plane more fully.

on this grid results in the *dirty image* of $I(l,m)$, i.e., $I(l,m)$ convolved with the FFT of S.

The shape of S can be very uneven, and as such the resulting Fourier transform can contain strong peaks that are off from the main peak. This will introduce false sources in the dirty image and distort the shape of sources. To avoid this we can use a deconvolution algorithm, that attempts to remove the convolution. The most commonly used is CLEAN (Högbom 1974).

The limitation of any deconvolution algorithm is that there is no unique way to do this. There could be a number of different brightness distributions $I(l,m)$ that correspond to the same dirty image.

2.1.3 Wide field effects

For an observation with a large FOV, it is important to consider how the array appears for sources away from the phase centre. To do this properly, we need to describe the array in its full three dimensional configuration. This is done by adding a third coordinate w describing the separation of the telescopes along the line of sight. Equation 2.4 can then be expanded to

$$V(u,v,w) = \int_{\text{sky}} \frac{A_N(l,m)I(l,m)}{\sqrt{1-l^2-m^2}} e^{2\pi i\left[ul+vm+w\left(\sqrt{1-m^2-l^2}-1\right)\right]} dl dm. \qquad (2.6)$$

Equation 2.6 does not describe a 2D Fourier transform. We can not image this using the same method as equation 2.4. Instead we can use the *w-projection* algorithm (Cornwell et al. 2008). This grids the uv-plane for several different values of w and combines them into one image. This allows producing correct images for larger FOVs.

2.2 Common models in the uv-domain

An alternate approach to find $I(l,m)$ is *model fitting*. This relies on a parametric description of the observed target, which can be represented directly in the uv-domain. Using a minimization algorithm, a set of values for the parameters is then found that minimizes the difference between the model and the observed visibilities. Model fitting will be discussed in more detail in chapter 3. This section will discuss the representations of various common source models in the uv-domain.

The simplest model is the *point-source model*, where $I(l,m)$ is described by a simple Dirac delta

$$I(l,m) = \Phi\delta(l-l_0, m-m_0) \qquad (2.7)$$

where Φ is the flux density of the source, (l_0, m_0) are the coordinates of the source. Inserting this into equation 2.6 we obtain

$$I(l, m) = \Phi A_N(l_0, m_0) \frac{e^{2\pi i \left[ul_0 + vm_0 + w\left(\sqrt{1 - l_0^2 - m_0^2} - 1\right)\right]}}{\sqrt{1 - l_0^2 - m_0^2}}. \tag{2.8}$$

This consists of three parts: the flux-density term Φ, the primary beam attenuation $A_N(l_0, m_0)$, and a translation. The translation will be referred to as ξ in the rest of this thesis

$$\xi_{(l_0, m_0)}(u, v, w) = \frac{e^{2\pi i \left[ul_0 + vm_0 + w\left(\sqrt{1 - l_0^2 - m_0^2} - 1\right)\right]}}{\sqrt{1 - l_0^2 - m_0^2}}. \tag{2.9}$$

Note that $\left|\xi_{(l_0, m_0)}(u, v, w)\right|$ is constant for all (u, v, w), and Φ is constant for a point source.

Another common model is the Gaussian model, defined as

$$I(l, m) = \frac{\Phi}{2\pi\sigma^2} e^{-\frac{(l - l_0)^2 + (m - m_0)^2}{2\sigma^2}}, \tag{2.10}$$

where σ is the size of the source, Φ is the total flux density, and (l_0, m_0) are the coordinates of the peak. The size of Gaussian is often described in terms of the full-width half-maximum (FWHM) instead of σ, which can be calculated as FWHM $= 2\sqrt{2\ln 2}\sigma \approx 2.35\sigma$. If we assume that $\sigma \ll \frac{\lambda}{D}$, we can approximate $A_N(l, m)$ as constant, and arrive at the following model in the uv-domain:

$$V_{\text{Gaussian}}(u, v, w) = \Phi A_N(l_0, m_0) e^{-2\pi^2\sigma^2(u^2 + v^2)} \xi_{(l_0, m_0)}(u, v, w). \tag{2.11}$$

Note that if $\sigma^2(u^2 + v^2)$ is small for all sampled (u, v) then equation 2.11 becomes equation 2.8. This can be generalized and all sources that are significantly smaller than the resolution can be well approximated as point sources.

As discussed in section 1.6 another commonly used intensity profile for galaxies is the Sérsic profile, defined in equation 1.10. This profile does not have a simple analytic description in the uv-domain for all n. Instead we use a numerical approximation in this work, based on a spline interpolation of the numerical FFT of the Sérsic profile. In Fig. 2.3 we show a typical Sérsic and Gaussian profile in the uv-domain. In comparison to the Gaussian profile, the Sérsic profile has a larger contribution at longer baselines for a given size, especially for large n.

2.3 Stacking in the uv-domain

For the models of the Gaussian and the point source, as long as the size is significantly smaller than the FOV, the translation and spatial extent are separable in the uv-domain. We define the inverse of the translation $\xi_{(l_0, m_0)}^{-1}(u, v, w) =$
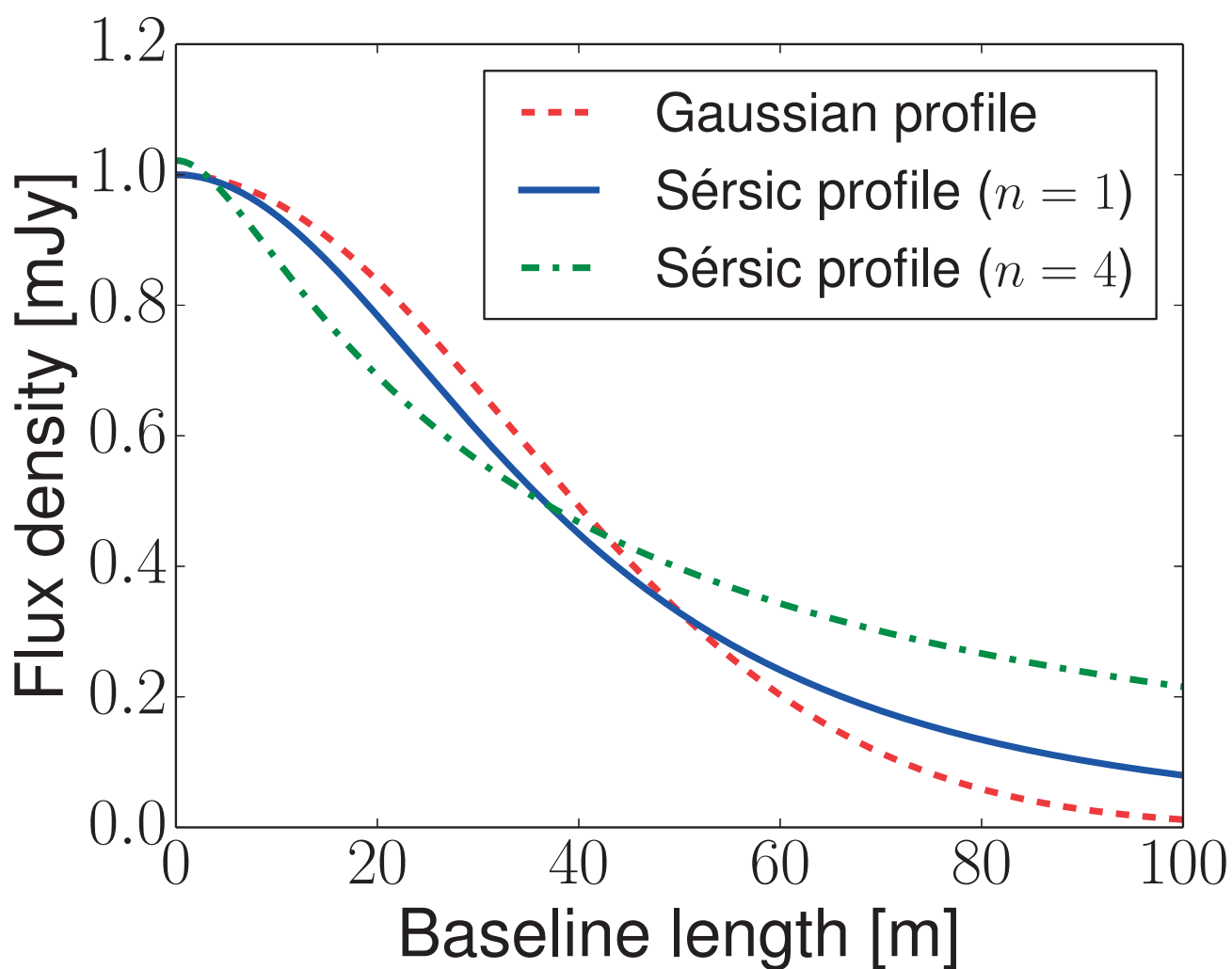
Figure 2.3: Model $V(\sqrt{u^2 + v^2})$ for a Gaussian and two Sersic profiles for a source at frequency 345 GHz with $R_e = 1''$ and $\Phi = 1$ mJy. For the Gaussian profile $R_e = \frac{\text{FWHM}}{2}$.

$\xi_{(-l_0,-m_0)}(u,v,w)$. By multiplying each visibility with ξ^{-1} we will move a given source into the phase centre.

By using $\xi_{(l_0,m_0)}^{-1}(u,v,w)$ we can perform stacking in the uv-plane. For each target position we create a copy of the full uv-data, then we centre the position of interest by multiplying with $\xi_{(l_i,m_i)}^{-1}(u,v,w)$ where (l_i, m_i) are the coordinates of the stacking positions. After centring we can average the visibilities of each source to produce a new set of visibilities with an averaged (or stacked) version of our target sources. To produce an accurate flux density we must also correct for A_N for each source. This results in a larger noise for sources far from the original phase centre. To minimize the noise in the final stacked data set we can use weighted average, assigning a set of weights $W_i^{(\text{stack})}$ for each position. Note that these are separate from the weights that are associated with each visibility. Combining all these effect and reordering the terms we arrive at the following expression to describe the uv-stacking algorithm

$$V_{\text{stack}}(u,v,w) = V(u,v,w) \frac{\sum_{i=1}^{N} W_i^{(\text{stack})} A_N^{-1}(l_i,m_i) \xi_{(l_i,m_i)}^{-1}(u,v,w)}{\sum_{i=1}^{N} W_i} \qquad (2.12)$$

where N is the total number of stacking positions. The simplest version of weighting accounts for the primary beam attenuation, i.e., $W_i^{(\text{stack})} = A_N(l_i,m_i)^2$.

Stacking by this method is limited by the fact that it does not allow to shift the (u,v,w) for different positions. This shift is a smaller effect than the phase correction $w(\sqrt{1-dx^2-dy^2}-1)$. For the VLA field of view of $30'$ at $1.4\,\text{GHz}$ the shift in u and v will be typically less than a few per cent in each. Neither does the shift in (u,v,w) affect the total flux measured for our source, rather it changes the shape of the stacked source. This size error is close to the typical change in u and v, i.e., less than a few percent for VLA at $1.4\,\text{GHz}$ and significantly smaller for ALMA.

2.4 Introduction to Paper I

Paper I is a discussion on stacking for interferometric data sets. It compares the uv-stacking technique described in Section 2.3, to a more conventional image based stacking. Using a wide array of realistic simulations it finds that image and uv-stacking generally produce consistent results. However, for data sets where very bright interfering sources are present, the image stacking is significantly more challenging with typically larger errors and significant biases in the stacking.

The project to develop an algorithm to stack in the uv-domain was initiated by Kirsten Knudsen and Wouter Vlemmings. I developed the uv-stacking algorithm and performed the suite of simulations in the paper. The paper was

written up by me in collaboration with Kirsten Knudsen, and improved based on discussion and feedback from the co-authors and an anonymous referee.

2.4.1 Simulation details, method of generation of sources.

Simulated data are used to test the stacking algorithm. The simulated data are produced to mimic real data. This means that the data will not only contain the target sources, but also a population of other sources such that the full distribution of sources mimics what would be seen in a real observation. Due to noise on each visibility, it is impossible to fully deconvolve or remove the bright sources. Especially for VLA, due to its large field of view, which ensure many bright sources in each field of view. This means that the noise, even after deconvolution, will have a significant contribution from the side lobes of bright sources. As such, the flux distribution of the bright sources is important for the noise characteristics.

To produce data sets that mimics real data set we introduce two separate populations of sources into the data. We introduce one population of brighter sources, with the aim to achieve a good over all flux distribution. The second population we introduce is our target population. The target population consists of galaxies that are too faint to be individually detected and this population is used to evaluate our stacking algorithms.

In Paper I we simulate 1.4 GHz VLA observations and 230 GHz ALMA cycle 1 observations. All sources are generated using a Gaussian model, with coordinates (l_k, m_k), total flux densities S_k, and sizes σ_k. The sources are inserted directly into the uv-domain using equation 2.11. When the size of the source approaches zero $I(l, m)$ approaches a two dimensional Dirac delta function $\delta(l - l_k, m - m_k)$. To avoid numerical imprecision when size is 0, $V(u, v, w)$ is replaced with a corresponding point-source model.

The coordinates (l_k, m_k) are generated uniformly in the FOV, i.e., $l_k = U(-0.5, 0.5) \times$ FOV and $m_k = U(-0.5, 0.5) \times$ FOV where $U(\text{lower}, \text{upper})$ is a function that generates pseudo random numbers in the interval [lower, upper] with a uniform distribution. The phase centre is set to $(57.2957795°, -30°)$ for all simulations. The declination $-30°$ was chosen to be similar to the declination of the Extended Chandra Deep Field-South (ECDFS). The right ascension was chosen at random as it does not impact on the data. To generate the flux densities S_k, we use flux-density distributions from observations of real sources. From the flux-density distribution we generate a cumulative distribution function F. This function is then modelled with a 2D spline to allow us to calculate the inverse function F^{-1}. The flux densities of our sources are then generated with $F^{-1}(U(0, 1))$. The exact form of F for our populations will be defined below.

2.4.2 Lyman-break galaxies

For VLA we used a target population mimicking Lyman-break galaxies (LBGs). The luminosity function of LBGs is typically modelled in the rest frame ultraviolet by a Schechter function (Schechter 1976), e.g., Steidel et al. (1999); Bouwens et al. (2007). Note that this is the luminosity function and not the flux-density distribution. Doing this it is assumed that all LBGs are at similar distances.

The Schechter function is defined as

$$n\left(L/L_*\right)dL = \Phi^*(L/L_*)^\alpha e^{-L/L_*}dL, \tag{2.13}$$

where n is the differential number density of galaxies for a given luminosity, L_* is the characteristic galaxy luminosity, and Φ^* is a normalisation for the overall space density. The free parameter α describes the low luminosity slope in a $\log n$, $\log S$ plot and a Schechter function with $\alpha = -1$ is called flat. Bouwens et al. (2007) measured α and L_* for LBGs from $z \sim 3$ to $z \sim 6$, they found values of $\alpha \approx -1.7$. It is important to note that at this α the number of low luminosity galaxies is infinite. As such is it only valid in a limited interval, and the distribution must be normalised in this interval.

The ultraviolet luminosity traces the star formation rate of the LBGs. Since the radio continuum flux density traces the same star formation we expect a similar luminosity function. Guided by this we generate target sources using a Schechter function with α and Φ^* as measured by Steidel et al. (1999). This results in a cumulative distribution function

$$F(S) = \int_{0.1S_*}^{S} (x/S_*)^\alpha e^{-x/S_*}dx \left/ \int_{0.1S_*}^{\infty} (x/S_*)^\alpha e^{-x/S_*}dx \right. \tag{2.14}$$

where S is the flux density and x is the integration variable for the differential flux-density distribution. We estimate S_* (flux-density distribution scaling, equivalent to L_*) from Carilli et al. (2008), where they estimate the flux density from LBGs using stacking. To avoid divergence at low luminosity we generate no sources below $0.1L_*$, this is similar to the detection limit in Steidel et al. (1999). The parameter Φ^* is used to determine the number of sources to be generated in our field of view.

2.4.3 Radio flux-density distribution

The Schechter function only describes the flux density of our faint star-forming galaxies. In a real map we will have a large number of bright sources, the distribution of these sources strongly impact the statistics in the map. As such it is important to not leave them out when we generate our simulated data sets.

In contrast to the faint star-forming galaxies, we can measure the flux density of the bright sources directly. Bondi et al. (2008) examined the flux-density

distribution of radio sources at 1.4 GHz in the COSMOS field. They fitted the flux-density distribution of sources down to 11 µJy, describing $\log n$ in terms a 6th order polynomial in $\log S$. Note that this describes the flux density distribution rather than the luminosity function. Determining the luminosity function here would require to determine the redshift of our sources. This is not required in this context since only the flux-density distribution is of interest. As such we use the cumulative distribution function

$$F(S) = \int_{0.06\,\mathrm{mJy}}^{S} x^{-2.5} 10^{\left[\sum_{q=0}^{6} S_q \log 10(x)\right]} dx \bigg/ \int_{0.06\,\mathrm{mJy}}^{1\,\mathrm{Jy}} x^{-2.5} 10^{\left[\sum_{q=0}^{6} S_q \log 10(x)\right]} dx$$

(2.15)

where x is the integration variable for the differential flux distribution and S_q are the polynomial coefficients from Bondi et al. (2008).

2.4.4 Submm flux-density distribution

At submm wavelengths, most surveys are performed using single-dish telescopes with significantly lower resolution than ALMA. The distribution for ALMA may be different. Béthermin et al. (2012) studied the distribution of star-forming galaxies, to estimate flux-density distributions in ALMA bands. Hatsukade et al. (2013) observed with band 6 in ALMA cycle 0, and their results are consistent with the Béthermin et al. (2012) model. Therefore, we use the Béthermin et al. (2012) flux-density distribution to generate data sets. The cumulative distribution function is generated numerically from galaxy count table.

We simulate observations for ALMA with multiply pointings, both contiguous and non-contiguous mosaics. The latter are motivated by surveys such as the ALESS survey by Hodge et al. (2013), where known bright sources are targeted with ALMA. To simulate this we generate sources over a large field. The brightest sources are selected and the simulated data set has pointings centred at these. The fainter target sources are only generated inside these pointings.

Chapter 3

Model fitting and error estimates

As mentioned in section 2.2, instead of using FFT imaging and cleaning to obtain an approximation of $I(l, m)$, it is possible to fit a model directly in uv-domain. This have several advantages. Primarily, it allows robust analysis of errors on the fitted parameters, in contrast to imaging where the errors are often less well understood. In this chapter we will discuss a general procedure to perform model fitting in the uv-domain, and some of the techniques that can be used to analyze the errors.

3.1 χ^2 minimization

A common method to perform model fitting is by minimizing

$$\sum w^{(\mathrm{vis})} \left(\Re(V - V_{\mathrm{model}}) \right)^2 + \left(\Im(V - V_{\mathrm{model}}) \right)^2 \tag{3.1}$$

where V is the complex visibility and $w^{(\mathrm{vis})}$ is the corresponding visibility weight to V. The function $\Re$ and $\Im$ are used to designate the real and imaginary part of complex numbers. This is summing over all available visibilities, with flagged visibilities given a weight of 0.

A commonly used minimization algorithm is the Levenberg-Marquardt algorithm (Levenberg 1944). This algorithm exists in many open source implementation, most commonly used is probably the `MINPACK` package developed by University of Chicago, as Operator of Argonne National Laboratory. `MINPACK` is used as the underlying implementation in the python package scipy. However, as the size of modern interferometric data sets have increased, `MINPACK` has grown unyielding. More modern implementations exist. In this work model fitting was primarily performed using `Ceres`, a modern c++ implementation developed by engineers at Google (Agarwal et al. 2016)[1].

---

[1]ceres-solver.org

3.1.1   Gridding as performance optimization

It is possible to speed up model fitting by using gridding, where the visibilities are averaged upon a predefined grid. Doing this significantly reduces time required to calculate χ^2.

The are several limitations of gridded data. Firstly, it limits the resolution of (u, v) to the grid resolution, which is especially limiting for large FOVs. However, there are cases where this limitation is not as important. E.g., fitting the size of a source close to the phase centre. Since the emission away from the phase centre is not of interest, the model can be expected to vary slowly with (u, v). Secondly, gridding will not evenly sample the visibilities. Some grid cells will be highly sampled, while others may not have been sampled at all. If the cells are not weighted correctly this can produce very unreliable results, where a few outliers in an ill sampled grid point completely dominate the fit.

There are also several advantages to gridded data. The first is the major speedup that is usually the main motivation behind gridding. Secondly, in the case of fitting a source close to the phase centre, large grid cells can be used. Since the phase of sources far from the phase centre will vary quickly, such sources will typically be averaged away in large grid cells. This can reduce the impact of these source on the fit. Thirdly, the gridded data is much easier to interpret for a human. In Paper II the gridded data is overlayed with the fits, even if the fits where performed to the full data, as it gives an indication to the behaviour of the visibilties. Looking at the non-gridded visibilties, the signal will be drowned in the noise.

3.2   Error estimation techniques

In this section I describe some techniques that can used to estimate errors in stacking and model fitting.

3.2.1 χ^2 variation estimates

A simple method to estimate the error of a model fitting result, is to look at the variation of χ^2 as a function of the fitted parameters. If the errors of the visibilities follow Gaussian distribution the χ^2 should follow the χ^2 distribution. This implies, that for a model with 2 free parameters, if one parameters is varied such that χ^2 is larger by 2.3 compared to the minimized χ^2, the parameter deviates by 1σ from the fitted value. However, for a two parameter model, both parameters must be varied together to find a correct error estimate. Only varying one parameter at the time will fail if the parameters are co-dependent. A common method to do this is to evaluate χ^2 on a fixed grid, where each dimension of the grid corresponds to a parameter.

While this is generally a powerful method for simple error estimates, it has several weaknesses. It assumes a Gaussian distribution of the errors in the visibilities, and does not robustly handle outliers. A few very large visibilities can significantly offset the result and the error, without any signature in this error estimate. Another weakness is for models with larger number of free parameters. The calculation of the fixed grid scales as N^k, where N is the size of the grid and k is the number of free parameters. This results in a very slow calculation if k is large.

3.2.2   Monte-Carlo simulations

Another method to estimate the errors is to simulate a data set based on a model of the fitted source, and performing the same model fit on the simulated data set. By performing multiple simulations we can study the distribution of each parameter, which will allow us to understand the error factors. This will work even if the errors do not follow a normal distribution. It is important that the method used to simulate the fake data sets include all effects that may contribute to the noise, and also that the simulations are produced in a manner that ensure that the error effects are independent between the different simulations.

Monte-Carlo simulations for single sources

`CASA` provides a frame work to produce simulated data sets in the task `simalma`. This task is primarily designed to simulate ALMA observations, but can also be used for other telescopes such as VLA as well. Using this task allows us to generate fully independent data sets. Many real observations will contain nearby bright sources that are not the target of the study, but can significantly impact the result. If this is the case, it is important to simulate a good approximation of such sources. If the data size is large this can become numerically challenging.

An alternate approach to full simulation is to introduce new sources into the original data set and model those. A typical ALMA or VLA observation will contain parts of the targeted sky with no sources present above the noise level. This is significantly faster than generating the data sets from scratch, and will also ensure that the noise is realistic.

Monte-Carlo simulation for stacking

It is possible to perform Monte-Carlo simulations for stacked sources in the same manner as for the version with only one source, however, it is generally better to include the stacking in the simulation. That is to generate a set of sources that individually fall below the noise level, stack them and model the

stacked data set. Apart from being more robust, this allows modelling of variation in the target stacking sources. E.g., if the sources have varying sizes this can be included as given each simulated sources a random size.

3.2.3 Bootstrapping

Bootstrapping is a more general statistical method. In this work the method is described in general first, with more specific applications to model fitting and stacking later.

In statistics, bootstrapping is a class of algorithms, which work through random sampling (with replacement). By studying how a measured quantity varies over different resamplings, a distribution for the quantity can be obtained. Since the resampling is performed without resampling, it is possible to produce $\binom{N \times 2 - 1}{N}$ unique resamples. Even for moderate size N this results in a large number, which means that an exhaustive search is generally not feasible. Instead a Monte-Carlo search can be used where 1000 or 10000 random resamples are evaluated.

Bootstrapping assumes that the sample is randomly selected, it will not estimate errors due to systematic selection biases. It does, however, not make any assumption on the underlying distribution of the factors that contribute to the errors.

Example: height of a group of people

As an example, the heights of 20 individuals are measured in cm and the follow values are found

$$X = (\quad 179.79, 195.81, 174.22, 180.10, 176.86, 191.13, 192.04, 188.12, 169.87,$$
$$177.14, 188.34, 180.66, 175.64, 194.07, 183.28, 167.60, 180.08, 188.42,$$
$$186.10, 180.12)$$

The average height of this sample of the population is 180.6 cm. To determine the accuracy of this value as an estimate of the entire population bootstrapping can be performed. To perform a resample, values are drawn from the sample. e.g.,

$$X_{\text{resample}} = (\quad 174.22, 180.10, 188.34, 175.64, 176.86, 188.42, 188.42, 188.12,$$
$$195.81, 194.07, 188.12, 195.81, 179.79, 179.79, 180.12, 175.64,$$
$$180.12, 179.79, 175.64, 186.10)$$

Note that the heights of individuals 6, 7, 9, 10, 12, 15, 16, and 17 from the original sample does not occur in this resample, while the heights of individuals 1, 2, 8, 13, 18, and 20 occur multiple times. The average height of this resample is also 182.5 cm. The sample is resampled 10000 times and the average height is calculated for each resample. This results in a distribution of values, as shown in Fig. 3.1. Based on the bootstrap and can be seen that the
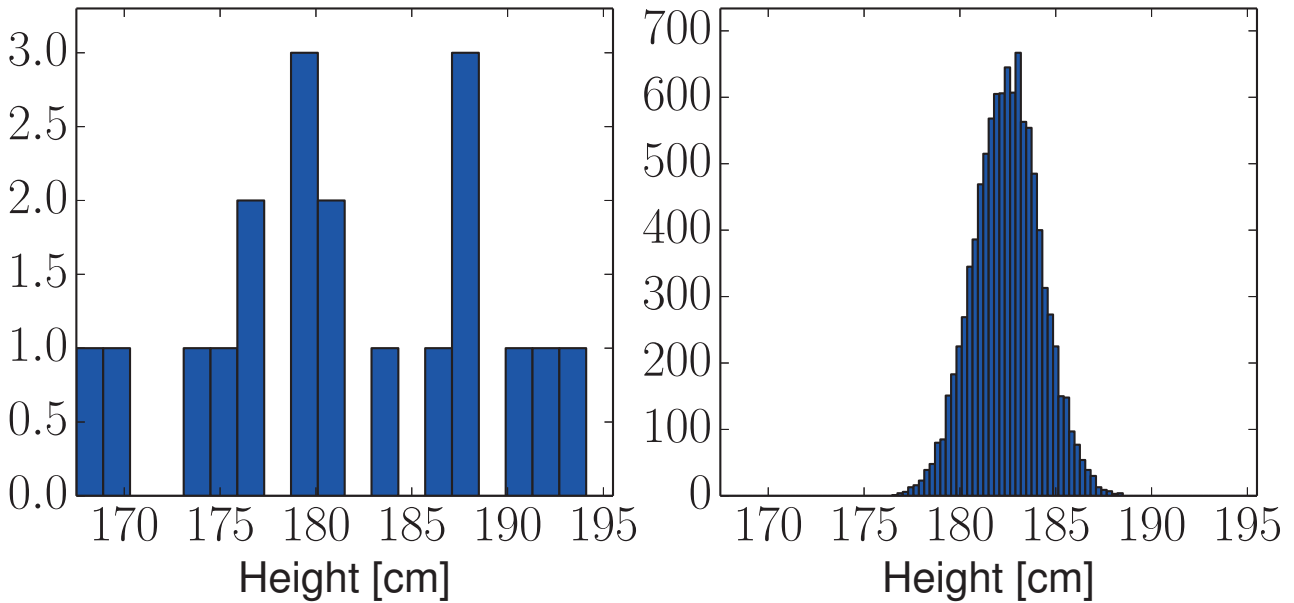
Figure 3.1: Example of the height of 20 individuals and bootstrapping of the mean for the sample. (Left) The distribution of the 20 sampled heights. (Right) The bootstrap distribution of the mean for 10000 resamples.

height values are drawn from a Gaussian distribution. From this distribution it can be determined that the height of the population is 182.5 ± 0.96 cm. In this example, the measured heights of individuals were randomized following the distribution for male adult in Sweden, a normal distribution with average of 181.5 cm.

Using bootstrap it is also possible to study other parameters, such as the standard deviation of the population. Fig. 3.2 shows the distribution of the standard deviation for the same resamples. This indicates that the standard deviation of the population is 7.67 ± 0.96 cm. The "true" value used when generating the given distribution was 7 cm.

Visibility bootstrapping

The bootstrapping technique can be used to estimate the uncertainties of any measured quantity for a uv data set by resampling the visibilities. For instance, Fig. 3.3 show an estimate of the fitted size of a source based on bootstrapping. The bootstrapping distribution has a tail towards larger sizes, however, around the mode of distribution it follows a Gaussian probability density function. The tail is consistent with a small number of outliers in the visibility data, and the distribution indicate that the measured size is robust. Based on the distribution we can compute uncertainties. Using an algorithm such as the one described by Cunnane (1978), we can compute the quantiles of the distribution
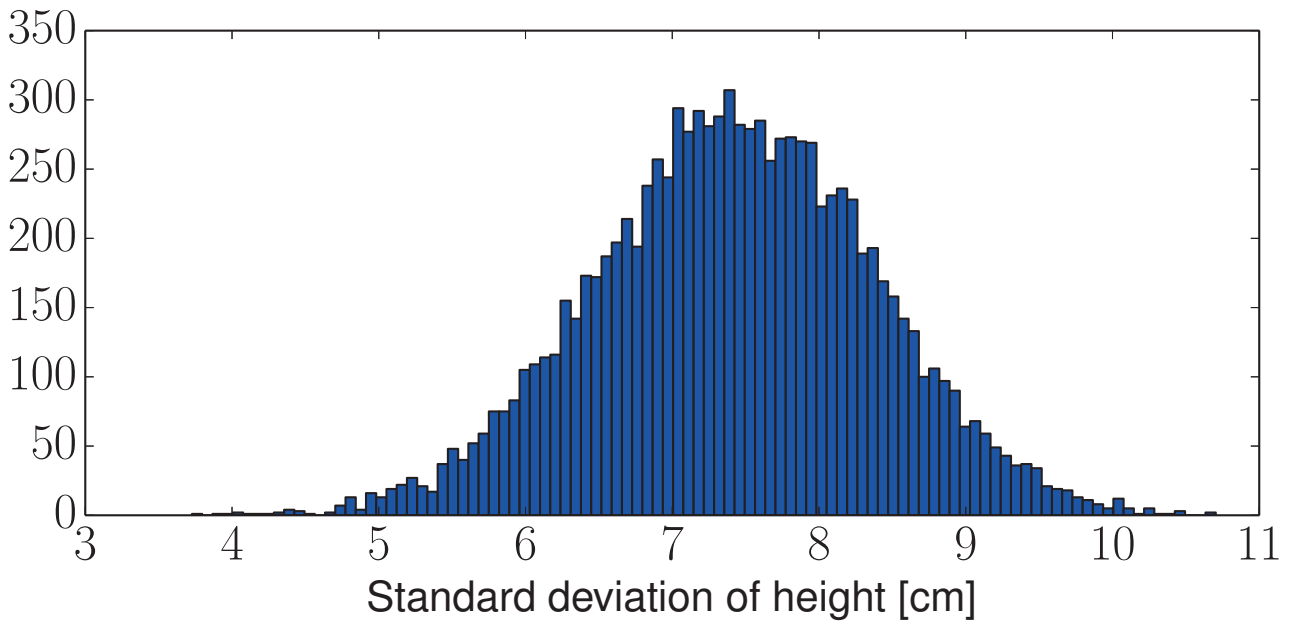
Figure 3.2: Example of the standard deviation of a population estimated from a sample of 20 individuals. The histogram shows the bootstrap distribution.

based on the cummulative distribution function (CDF). The quadrants where $\mathrm{CDF}(x) \approx 0.1587$ and $\mathrm{CDF}(x) \approx 0.8413$ correspond to $\pm 1\sigma$ for a Gaussian distribution, and will produce uncertainties with equivalent confidence. For the example in Fig. 3.3 this results in a size of $0\rlap{.}''94^{+0\rlap{.}''31}_{-0\rlap{.}''44}$.

Bootstrapping for stacking

When measuring the uncertainties of a stacked value, it may be preferable to resample the stacking sample in place of the visibilities of the stacked sample. Visibility stacking is accurate to estimate the error of a fitted parameter. However, for stacking the aim is to measure the average properties of a population. If the sample does not fully cover the target population, this will add uncertainties to the measured average properties. If the sample can be assumed to unbiased resampling the sample can account for this effect also.

E.g., take a sample of 400 galaxies. If stacking and visibility bootstrapping is used to measure the SFR of these galaxies, this will determine the answer to the question: "What is the average SFR of these 400 galaxies?" If the 400 galaxies are assumed to be a random subsample of the population of star-forming galaxies (at the given redshift and stellar mass). It is possible, by performing bootstrapping with resampling in the stacking sample, to answer the different question: "What is the average SFR of the population the 400 galaxies belong to?"
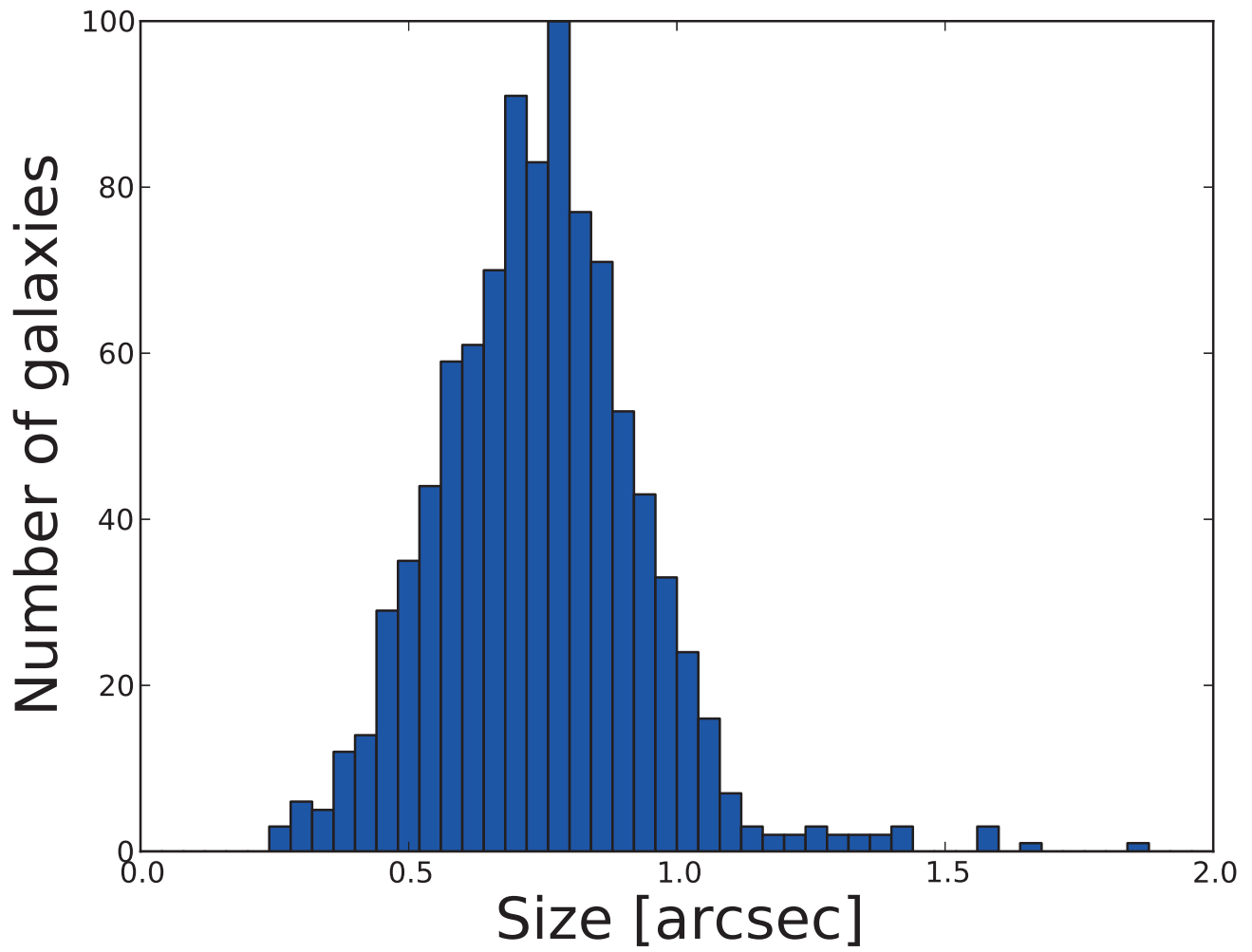
Figure 3.3: A estimates of uncertainty of a fitted size for a source in an interferometric data set. The estimate is based on bootstrapping of the visibilties.

For a large sample of galaxies, the measurement uncertainties are expected to be the dominant factor. However, for a small sample the sample bootstrapping may give significantly larger uncertainties, as compared to visibility bootstrapping.

3.2.4   Sample bias and other statistical biases

All the methods discussed in this section, assumes that the sample is random. This may not be the case. E.g., look at sample of galaxies selected from a specific deep field. If the deep field is small and the galaxies are selected in a narrow redshift range, it is possible that the galaxies belong to the same gravitationally bound structure. This could imply similar properties for these galaxies, and that these galaxies can no longer be seen as representative for a larger population of galaxies. Such effects has to be estimated by looking more at the details of a specific sample selection, and can generally be reduced by increasing sample size and selected galaxies from different deep fields.

Another bias that is generally present in all studies of high redshift galaxies is the calibration of indirect measurements of properties, such as the SFR. For instance by selecting different IMFs, the measured SFR can vary by approximately a factor 2. If we are comparing different populations of galaxies, ensuring to keep the calibrations the same, these effects can be minimized. However, these effects are very important to consider if the absolute SFR is of interest.

Chapter 4

Sizes of high-z galaxies

In this chapter I discuss the sizes of galaxies, especially high-z galaxies. In this thesis size is typically taken to mean effective radius of a galaxy, i.e., the radius that includes half the light of the galaxy. This is common in galaxy evolution studies (e.g. Conselice et al. 2014; Morishita et al. 2014; van der Wel et al. 2014), however, it is quite different from how size is defined for an object on Earth with fixed boundaries. An effect of the effective radius definition of size is that if we add more stars in the centre of a galaxy, the size of the galaxy shrinks. Not because the outer stars are pulled closer to the centre of the galaxy, but because a smaller radius can include half the light of the galaxy.

Observations of surface flux densities at optical wavelengths, such as the *HST* deep fields, are primarily sensitive to the stars in galaxies. In this work I will refer to sizes derived from such measurements as *optical sizes*. Even within the definition of optical sizes there are wavelength dependent effects. Star-forming galaxies have been found to be redder in the centre (e.g. Szomoru et al. 2011), which results in smaller sizes if the sizes are measured at longer wavelengths. Using the *HST* filters F125W and F160W van der Wel et al. (2014) estimated this effects, and found sizes measured between the two bands to differ with up to 10%, but smaller for lower masses and higher redshifts. Based on these measurements they define a scheme that can be used to calibrate the sizes for a fixed rest-frame wavelength.

As discussed in 1.4.5, a strong size evolution is seen for star-forming galaxies, with $\beta \approx -0.75$. A proposed mechanism to drive this size evolution is inside-out growth, where new stars are formed at the outer parts of the disks in the galaxies. The colour gradient observed by Szomoru et al. (2011) offer some support for this theory, as older stars are typically redder. However, dust extinction could also play a role in the gradient.

A more direct way to evaluate the role of star formation as a driver of size evolution is to map a tracer of the SFR. Based on the stellar-mass surface density
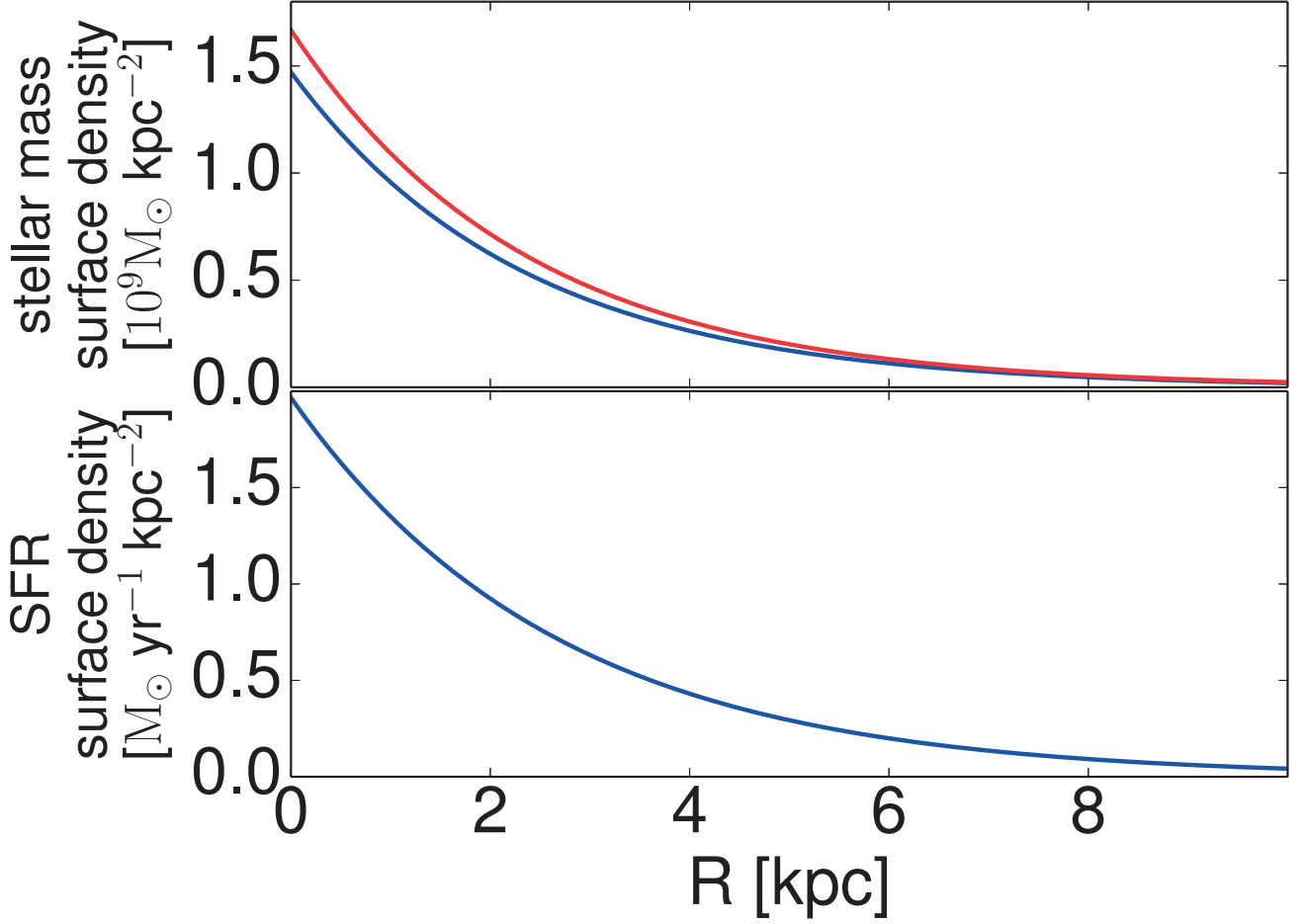
Figure 4.1: Radial profiles for Σ_{M_*} and Σ_{SFR} at $z \approx 2$ and $M_* \approx 5 \times 10^{10} \mathrm{M}_\odot$. (top) Two radial profiles for Σ_{M_*} for one model galaxy at two different times. The blue curve assumes $M_* = 5.0 \times 10^{10} \mathrm{M}_\odot$ and $R_e = 3.90$ kpc. The red curve is the same model galaxy, evolved for 10 Myr assuming SFR = 84 $\mathrm{M}_\odot \, \mathrm{yr}^{-1}$ (Speagle et al. 2014), and size evolution according to van der Wel et al. (2014). This results in $M_* = 5.8 \times 10^{10} \mathrm{M}_\odot$ and $R_e = 3.96$ kpc. (bottom) Radial profile of Σ_{SFR} calculated for the difference of the two above radial profiles.

(Σ_{M_*}) profiles, we can make some predictions for the SFR surface density (Σ_{SFR}). In Fig. 4.1 we show the radial profiles of Σ_{M_*} for a galaxy with $M_* = 5 \times 10^{10}$ M$_\odot$ at $z = 2$, using a typical radial profile of a galaxy at this redshift according to van der Wel et al. (2014), i.e., a Sérsic profile with $R_e = 3.9$ kpc and $n = 1$. We also show the radial profile of the same galaxy, evolved for 10 Myr, assuming a constant SFR = 84 M$_\odot$ yr^{-1} (Speagle et al. 2014), and size evolution according to van der Wel et al. (2014). In Fig 4.1 we also show the difference of the two profiles divided by 10 Myr, allowing us to estimate the typical Σ_{SFR} as a function of radius, assuming that star formation is the primary driver for size evolution. The resulting Σ_{SFR} profile also follow a Sérsic profile, with most stars forming in the centre of the galaxy, however, the size R_e is larger at ~ 4.5 kpc. Performing the same calculation for galaxies with $M_* = 5 \times 10^{10}$M$_\odot$ for a number of different redshift, we produce Fig. 4.2, that predicts the typical size of star-forming galaxies that would be measured using an SFR tracer assuming pure inside-out growth.

I this chapter I will discuss two SFR tracers, submm emission at 345 GHz and radio emission at 1.4 GHz. I will refer to the sizes derived with these two measures as *submm sizes* and *radio sizes*, respectively.

4.1 Distribution of galaxy sizes

In a population of galaxies no two galaxies are alike. While galaxies at high redshifts are generally smaller than lower redshift counterparts (e.g. van der Wel et al. 2014), there is a large scatter of sizes of galaxies at all redshifts. It is common to study the evolution of the median sizes of groups of galaxies, e.g. Morishita et al. (2014) study the median optical sizes of star-forming and quiescent galaxies. The median sizes are more robust compared to the average sizes in regards to large outliers, and avoid complications with assigning weights to different galaxies. Another approach is to fit a distribution to the sizes and study how the parameters of the distribution evolve. The PDF of the Rayleigh distribution is defined as:

$$f_{\mathrm{Rayleigh}}(R_e) = \frac{R_e}{\sigma^2} \exp\left(-\frac{R_e^2}{2\sigma^2}\right) \tag{4.1}$$

where σ is the scale parameter and the only free parameter of the distribution. For the log-normal distribution the PDF is defined as:

$$f_{\mathrm{log-normal}}(R_e) = \frac{1}{\sqrt{2\pi}R_e\sigma} \exp\left[-\frac{(\log R_e - \log \mu)^2}{2\sigma^2}\right] \tag{4.2}$$

where μ is the location parameter and σ is the scale parameter. The median is $\sqrt{2\ln 2}\sigma$ for the Rayleigh distribution and μ for the log-normal distribution, as
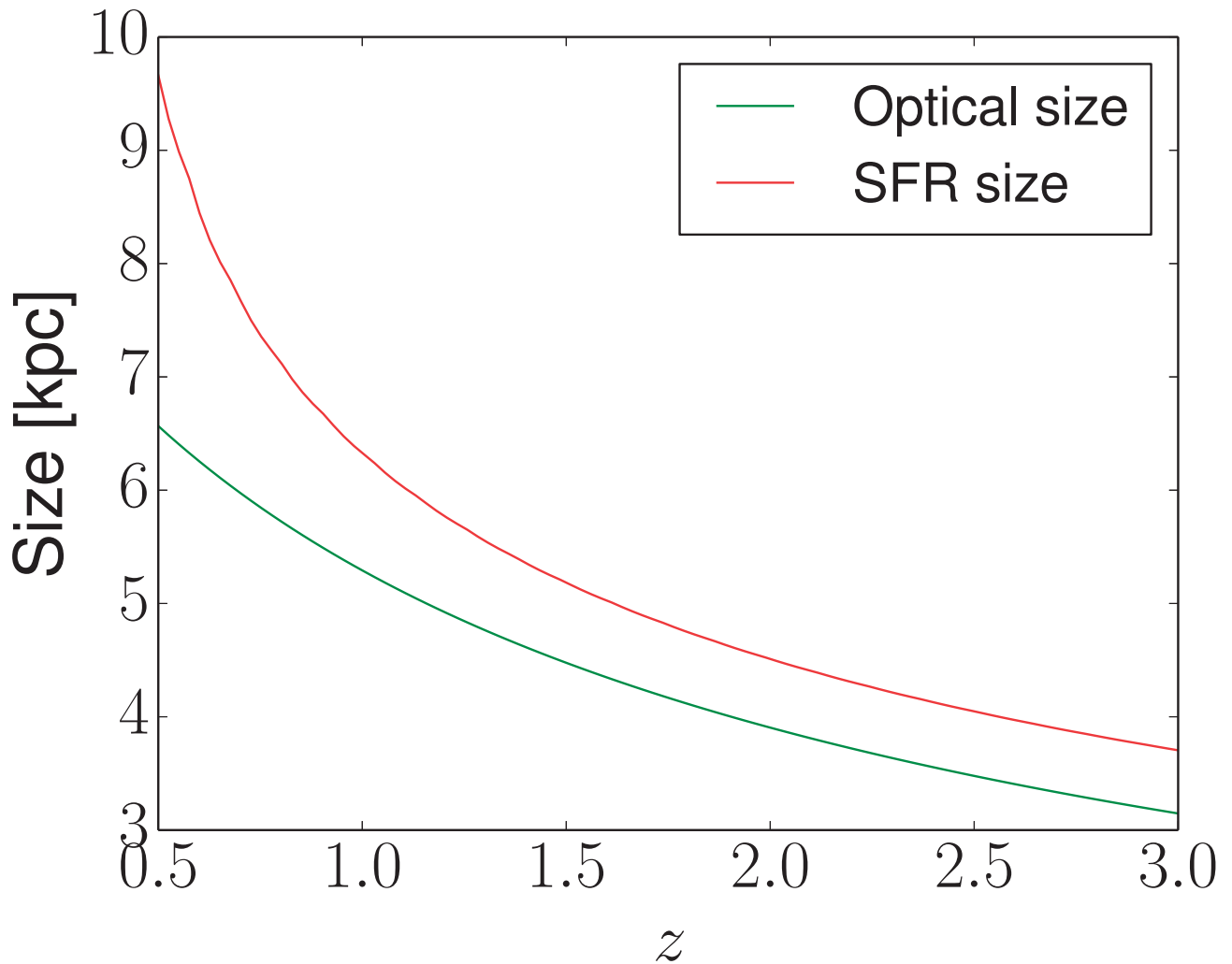
Figure 4.2: Predicted SFR sizes (radio and submm sizes) for a galaxy with $M_* = 5 \times 10^{10}$ M$_\odot$ assuming pure inside-out growth, i.e., the main driver of size evolution is formation of new stars. The predicted sizes are calculated using numerical differentiation of median radial profiles from van der Wel et al. (2014), with M_* evolving according to Speagle et al. (2014).

such studying the evolution of these parameters is largely equivalent to studies of the median size evolution. However, fitting a distribution it is possible to account for additional effects such as the uncertainties of individual sources. For the log-normal distribution we also have a second free parameter, which allow us to fit the variance of galaxy sizes within a population of galaxies. van der Wel et al. (2014) use the log-normal distribution to study the optical sizes of star-forming and quiescent galaxies. They find that σ is constant across different redshifts, with $\sigma \approx 0.13$ for quiescent galaxies and $\sigma \approx 0.17$ for star-forming galaxies, indicating that while the median size of galaxies does evolve, the overall shape of the distribution does not evolve as strongly. The scatter of the optical sizes measured for galaxies emphasises the importance of sufficiently large samples, or the results will not be representative of the population. However, it is important to note that the width of the distribution of sizes is smaller than the typical scatter of SFR around the star-formation sequence.

4.2 Evolution of optical sizes with redshift and stellar mass

Several studies have looked at the evolution of optical sizes as a function of z (e.g. Toft et al. 2007; Mosleh et al. 2012; Morishita et al. 2014; van der Wel et al. 2014). It is common to parametrize the size evolution as

$$R_e \propto (1 + z)^\beta. \tag{4.3}$$

For star-forming galaxies different studies find value of β between -0.6 and -1.1 (e.g. Toft et al. 2007; Franx et al. 2008; Mosleh et al. 2012; Morishita et al. 2014; van der Wel et al. 2014), with the highest values derived for LBGs (Mosleh et al. 2012). For quiescent galaxies the evolution is steeper, with studies finding β between -1 and -1.5 (e.g. Newman et al. 2012; van der Wel et al. 2014; Morishita et al. 2014). These measurements are generally based on samples of massive galaxies ($M_* \approx 10^{11} M_\odot$). van der Wel et al. (2014) study a sample of galaxies with M_* down to $10^9 M_\odot$ with the aim to study mass dependent effects. This allowed them to study how sizes depend on stellar mass across a range of redshifts. They found a weak dependence for star-forming galaxies $R_e \propto M_*^\alpha$ where $\alpha = -0.22$, and a much stronger dependence for quiescent galaxies with $\alpha \approx 0.74$. They found that the slope was constant across the sample redshift range from 0 to 3, for both star-forming and quiescent galaxies.

4.3 Evolution of submm and radio sizes

The prediction of submm and radio sizes in Fig. 4.2 is based on radial profiles of median galaxies, as measured from van der Wel et al. (2014). Accounting effects such at the distribution of sizes for different galaxies and changes in Sérsic n

complicate the picture. However, it is clear, that if the size evolution is primarily driven by star formation, the typical submm and radio sizes must be larger than optical sizes. If submm and radio sizes instead are smaller than optical sizes, galaxies should instead evolve towards smaller sizes at later times (lower redshift), in absence of other size evolution mechanisms. Note that smaller here means that the effective radius is smaller, and not that the outer parts are moving closer to the centre.

Most submm studies of sizes focus on submm galaxies (SMGs), galaxies selected by their high flux density at submm wavelengths. E.g., Simpson et al. (2015) measure the median FWHM size for a group of 23 submm galaxies at $z \approx 2.5$ to be $0\rlap{.}''3 \pm 0\rlap{.}''04$ (2.4 ± 0.2 kpc). Ikarashi et al. (2015) study a sample of SMGs at somewhat higher redshifts ($z \approx 4$) and find a median FWHM size of $0\rlap{.}''2^{+0\rlap{.}''03}_{-0\rlap{.}''05}$ ($1.4^{+0.2}_{-0.4}$ kpc). These submm sizes are significantly smaller than the optical sizes of typical star-forming galaxies, however, SMGs are not typical star-forming galaxies. E.g., the median SFR for the 77 SMGs in Simpson et al. (2014) is $840 \pm 120 \, \mathrm{M_\odot \, yr^{-1}}$, which is ~ 6 times higher than would have been expected if they followed the star-formation sequence. In Paper II and III present measurements for submm and radio sizes, for samples selected to be more typical star-forming galaxies.

4.4   Introduction to Paper II

Paper II presents measurements of submm sizes of star-forming galaxies at $z \approx 2$. The typical flux densities of the sources are too faint to be directly detected, and the sizes are measured by using uv-stacking and model fitting. The paper shows that using stacking it is possible to measure average submm sizes for the galaxies. Several samples of galaxies are selected based on optical and near-infrared bands. Looking at the sBzK galaxies, the average submm Gaussian FWHM size is found to be $0\rlap{.}''64 \pm 0\rlap{.}''17$. Considering the median $z \approx 2$, this corresponds to a physical submm size of 5.5 ± 1.5 kpc, or $R_e = 2.8 \pm 0.8$ kpc. In this paper we also measure the optical sizes at z-band of the same sBzK galaxies, finding median $R_e = 4.5 \pm 0.5$ kpc. This is similar to typical star-forming galaxies galaxies at the same redshift, e.g., the van der Wel et al. (2014) parametrization predicts median $R_e = 3.5$ kpc at $z = 2$. We note that while measured submm sizes are larger than those of SMGs, they are still small compared to optical sizes, and while the uncertainties are large, the measured sizes are not consistent with the submm sizes being significantly larger than the optical sizes. This seems to indicate that other processes than star formation are central in shaping the size evolution of star-forming galaxies.

This paper was based on an idea by John Conway to use the uv-stacking algorithm developed in Paper I to study sizes of stacked sources. I have per-

formed the uv-stacking analysis, model fitting and statistical tests based on the ALMA data provided by the ALESS collaboration. Based on the stellar mass estimates performed by Guillaume Drouart and the optical size estimates performed by Lulu Fan, I performed the analysis of the data. The paper was written up by me in collaboration with Kirsten Knudsen, and improved based on discussion and feedback from Robert Beswick, Ivan Martí-Vidal, Ian Smail, the co-authors, and an anonymous referee.

4.4.1 Future prospects

Paper II is based around stacking to estimate average properties of star-forming galaxies. The results of Paper II indicate that star-formation formation acts to concentrate the Σ_{M_*} radial profile towards the centre. To gain more detailed insight into how star formation influences size evolution, requires either significantly larger samples, or more detailed observations of individual sources. Larger samples are addressed in Paper III, however, for detail studies of star-forming galaxies ALMA is an ideal telescope. The high angular resolution, strong uv-coverage, and good continuum sensitivity allows robust resolved measurements of Σ_{SFR}. I am P.I. of a proposal to observe a sample of 30 star-forming galaxies, with $z \approx 2 - 3$ and $M_* \approx 10^{10.5} - 10^{11} M_\odot$. All the galaxies in the sample have high-resolution optical *HST* observations, allowing direct comparison to be made between Σ_{SFR} and Σ_{M_*} for each galaxy.

4.5 Introduction to Paper III

Paper III uses VLA data combined with data from the Multi-Element Radio Linked Interferometer Network (MERLIN) to measure radio sizes of star-forming galaxies. MERLIN is an interferometer with telescopes spread over England, with baselines out to 217 km. MERLIN has a significantly higher resolution compared to the VLA. Combining data from the two telescope ensure a good uv-coverage over a large range of baselines. Radio observations around 1.4 GHz lend themselves well for studies of large samples of galaxies, as the FOVs of interferometers at these frequencies are naturally large. Paper III uses galaxies selected from *HST* survey of the GOODS-N field centred at $12^h35^m54^s.98$ $+62°11'51''.3$ (Skelton et al. 2014). The MERLIN and VLA observations of the GOODS-N covers the majority of the 177 arcmin^2 covered by the Skelton et al. (2014) survey of the field. This allows us to study the radio emission of ~ 1000 galaxies with known photometric redshifts ($z = 0 - 3$) and stellar masses ($M_* = 10^{10} - 10^{11} M_\odot$). Paper III finds that radio sizes are typically half of the optical sizes for star-forming galaxies across the sampled redshift range. With the larger sample size compared to Paper II, the measured size difference is statis-

tically significant, clearly indicating that star formation can not drive size evolution.

The paper was initiated in collaboration with Robert Beswick, who performed image-stacking on galaxies in the MERLIN data. I performed a new sample selection based on the sample selection in van der Wel et al. (2014), and a new stacking analysis using the uv-stacking algorithms. The paper is written up by me in collaboration with Kirsten Knudsen, and improved based on feedback from the co-authors.

4.5.1 Future prospects

Paper III provides strong support for radio sizes being systematically smaller compared to optical sizes. The analysis in Paper III is based on MERLIN, before the recent upgrade of the array to e-MERLIN. As part of the e-MERLIN legacy programmes, the GOODS-N will be re-observed in the e-MERGE survey. The e-MERGE survey provides much deeper data compared to the old MERLIN observations of the field. In Paper III, radio size as a function of stellar mass was not studied, as the resulting uncertainty was too large for the result to be robust. Using the deeper e-MERGE data it would be possible to re-stack the samples, studying how radio size evolution varies with stellar mass.

The e-MERGE survey also includes observations at ~ 5 GHz. If the typical spectral indices are different in outer parts of the galaxies, compared the in centre of the galaxies, this could result in different sizes at 1.4 and 5 GHz.

4.6 Conclusions

Paper II and III indicate that if galaxies were left alone forming stars, sizes would tend to grow smaller, not larger, at later times. The radio and submm observations clearly show that the star formation is most efficient in the centre of the galaxies. However, this is not necessarily very surprising. As discussed in section 4.2, size evolution is strongest for quiescent galaxies, where very little star formation is taking place. It is possible that star-formation is acting to slow down size evolution in star-forming galaxies compared to quiescent galaxies. New telescopes and improving algorithms offers promises for a much deeper understanding of galaxy evolution in the future. As the results of Paper II and III demonstrate, the location of star formation in high-z galaxies plays a important role in this evolution. Resolved submm and radio continuum observations of high-z galaxies have a high potential to provide vital pieces of the puzzle of galaxy evolution.

Bibliography

Abramson, L. E., Gladders, M. D., Dressler, A., et al. 2016, ApJ submitted (arXiv: 1604.00016)

Agarwal, S., Mierle, K., et al. 2016, Ceres Solver, http://ceres-solver.org

Baldry, I. K., Glazebrook, K., Brinkmann, J., et al. 2004, ApJ, 600, 681

Beelen, A., Cox, P., Benford, D. J., et al. 2006, ApJ, 642, 694

Behroozi, P. S., Wechsler, R. H., & Conroy, C. 2013, ApJ, 770, 57

Béthermin, M., Daddi, E., Magdis, G., et al. 2012, ApJ, 757, L23

Bian, F., Stark, D. P., Fan, X., et al. 2015, ApJ, 806, 108

Blakeslee, J. P., Holden, B. P., Franx, M., et al. 2006, ApJ, 644, 30

Bondi, M., Ciliegi, P., Schinnerer, E., et al. 2008, ApJ, 681, 1129

Bouwens, R. J., Illingworth, G. D., Franx, M., & Ford, H. 2007, ApJ, 670, 928

Bouwens, R. J., Illingworth, G. D., Oesch, P. A., et al. 2012, ApJ, 754, 83

Bouwens, R. J., Illingworth, G. D., Oesch, P. A., et al. 2011, ApJ, 737, 90

Brinchmann, J., Charlot, S., White, S. D. M., et al. 2004, MNRAS, 351, 1151

Brown, M. J. I., Dey, A., Jannuzi, B. T., et al. 2007, ApJ, 654, 858

Buitrago, F., Trujillo, I., Conselice, C. J., & Häußler, B. 2013, MNRAS, 428, 1460

Capak, P., Aussel, H., Ajiki, M., et al. 2007, ApJS, 172, 99

Cardamone, C. N., van Dokkum, P. G., Urry, C. M., et al. 2010, ApJS, 189, 270

Carilli, C. L., Lee, N., Capak, P., et al. 2008, ApJ, 689, 883

Carrasco, E. R., Conselice, C. J., & Trujillo, I. 2010, MNRAS, 405, 2253

Chabrier, G. 2003, PASP, 115, 763

Chary, R. & Elbaz, D. 2001, ApJ, 556, 562

Cheung, E., Bundy, K., Cappellari, M., et al. 2016, Nature, 533, 504

Condon, J. J. 1992, ARA&A, 30, 575

Conselice, C. J., Bluck, A. F. L., Mortlock, A., Palamara, D., & Benson, A. J. 2014, MNRAS, 444, 1125

Consolandi, G., Gavazzi, G., Fumagalli, M., Dotti, M., & Fossati, M. 2016, A&A accepted, (arXiv: 1603.07753)

Cornwell, T. J., Golap, K., & Bhatnagar, S. 2008, IEEE Journal of Selected Topics in Signal Processing, 2, 647

Cucciati, O., Tresse, L., Ilbert, O., et al. 2012, A&A, 539, A31

Cunnane, C. 1978, Journal of Hydrology, 37, 205

Daddi, E., Cimatti, A., Renzini, A., et al. 2004, ApJ, 617, 746

Daddi, E., Dickinson, M., Morrison, G., et al. 2007, ApJ, 670, 156

Daddi, E., Renzini, A., Pirzkal, N., et al. 2005, ApJ, 626, 680

Dahlen, T., Mobasher, B., Dickinson, M., et al. 2007, ApJ, 654, 172

Dahlen, T., Mobasher, B., Faber, S. M., et al. 2013, ApJ, 775, 93

Dale, D. A., Beltz-Mohrmann, G. D., Egan, A. A., et al. 2016, AJ, 151, 4

de Vaucouleurs, G. 1948, Annales d'Astrophysique, 11, 247

Elston, R., Rieke, G. H., & Rieke, M. J. 1988, ApJ, 331, L77

Faber, S. M., Willmer, C. N. A., Wolf, C., et al. 2007, ApJ, 665, 265

Fabian, A. C. 2012, ARA&A, 50, 455

Finkelstein, S. L., Papovich, C., Dickinson, M., et al. 2013, Nature, 502, 524

Franx, M., Labbé, I., Rudnick, G., et al. 2003, ApJ, 587, L79

Franx, M., van Dokkum, P. G., Förster Schreiber, N. M., et al. 2008, ApJ, 688, 770

Fukugita, M. & Peebles, P. J. E. 2004, ApJ, 616, 643

Gawiser, E., van Dokkum, P. G., Herrera, D., et al. 2006, ApJS, 162, 1

Goldbaum, N. J., Krumholz, M. R., & Forbes, J. C. 2016, ApJ accepted, (arXiv: 1605.00646)

Gruppioni, C., Pozzi, F., Rodighiero, G., et al. 2013, MNRAS, 432, 23

Gültekin, K., Richstone, D. O., Gebhardt, K., et al. 2009, ApJ, 698, 198

Hatsukade, B., Ohta, K., Seko, A., Yabe, K., & Akiyama, M. 2013, ApJ, 769, L27

Hayward, C. C., Jonsson, P., Kereš, D., et al. 2012, MNRAS, 424, 951

Hildebrandt, H., Arnouts, S., Capak, P., et al. 2010, A&A, 523, A31

Hodge, J. A., Karim, A., Smail, I., et al. 2013, ApJ, 768, 91

Högbom, J. A. 1974, A&AS, 15, 417

Hubble, E. P. 1926, ApJ, 64

Ikarashi, S., Ivison, R. J., Caputi, K. I., et al. 2015, ApJ, 810, 133

Just, A. & Jahreiß, H. 2010, MNRAS, 402, 461

Karim, A., Schinnerer, E., Martínez-Sansigre, A., et al. 2011, ApJ, 730, 61

Kennicutt, Jr., R. C. 1998, ApJ, 498, 541

King, A. & Pounds, K. 2015, ARA&A, 53, 115

Leitherer, C. & Heckman, T. M. 1995, ApJS, 96, 9

Leitner, S. N. 2012, ApJ, 745, 149

Leslie, S. K., Kewley, L. J., Sanders, D. B., & Lee, N. 2016, MNRAS, 455, L82

Levenberg, K. 1944, Quart. Appl. Math., 2, 164

Madau, P. & Dickinson, M. 2014, ARA&A, 52, 415

Magnelli, B., Elbaz, D., Chary, R. R., et al. 2011, A&A, 528, A35

Magnelli, B., Popesso, P., Berta, S., et al. 2013, A&A, 553, A132

Marchesini, D., van Dokkum, P. G., Förster Schreiber, N. M., et al. 2009, ApJ, 701, 1765

Miller, N. A., Bonzini, M., Fomalont, E. B., et al. 2013, ApJS, 205, 13

Mo, H. J., Mao, S., & White, S. D. M. 1998, MNRAS, 295, 319

Morishita, T., Ichikawa, T., & Kajisawa, M. 2014, ApJ, 785, 18

Mosleh, M., Williams, R. J., Franx, M., et al. 2012, ApJ, 756, L12

Moustakas, J., Coil, A. L., Aird, J., et al. 2013, ApJ, 767, 50

Murphy, J. D., Gebhardt, K., & Adams, J. J. 2011, ApJ, 729, 129

Newman, A. B., Ellis, R. S., Bundy, K., & Treu, T. 2012, ApJ, 746, 162

Noeske, K. G., Weiner, B. J., Faber, S. M., et al. 2007, ApJ, 660, L43

Oesch, P. A., Brammer, G., van Dokkum, P. G., et al. 2016, ApJ, 819, 129

Oesch, P. A., van Dokkum, P. G., Illingworth, G. D., et al. 2015, ApJ, 804, L30

Ownsworth, J. R., Conselice, C. J., Mundy, C. J., et al. 2016, MNRASin press (arXiv: 1605.05741)

Patel, S. G., Holden, B. P., Kelson, D. D., et al. 2012, ApJ, 748, L27

Planck Collaboration, Ade, P. A. R., Aghanim, N., et al. 2014, A&A, 571, A16

Quadri, R., Marchesini, D., van Dokkum, P., et al. 2007, AJ, 134, 1103

Reddy, N. A. & Steidel, C. C. 2009, ApJ, 692, 778

Rees, M. J. & Ostriker, J. P. 1977, MNRAS, 179, 541

Robotham, A. S. G. & Driver, S. P. 2011, MNRAS, 413, 2570

Rocha-Pinto, H. J., Scalo, J., Maciel, W. J., & Flynn, C. 2000, A&A, 358, 869

Rodighiero, G., Daddi, E., Baronchelli, I., et al. 2011, ApJ, 739, L40

Sanders, D. B., Mazzarella, J. M., Kim, D.-C., Surace, J. A., & Soifer, B. T. 2003, AJ, 126, 1607

Schechter, P. 1976, ApJ, 203, 297

Schenker, M. A., Robertson, B. E., Ellis, R. S., et al. 2013, ApJ, 768, 196

Schiminovich, D., Ilbert, O., Arnouts, S., et al. 2005, ApJ, 619, L47

Sersic, J. L. 1968, Atlas de galaxias australes

Simpson, J., Swinbank, M., Smail, I., et al. 2014, ApJ, 788, 125

Simpson, J. M., Smail, I., Swinbank, A. M., et al. 2015, ApJ, 799, 81

Skelton, R. E., Whitaker, K. E., Momcheva, I. G., et al. 2014, ApJS, 214, 24

Song, M., Finkelstein, S. L., Livermore, R. C., et al. 2016, ApJ submitted (arXiv: 1602.02160)

Sparke, L. S. & Gallagher, J. S. 2007, Galaxies in the Universe – an introduction, second edition; 5th printing edn. (Cambridge University Press)

Speagle, J. S., Steinhardt, C. L., Capak, P. L., & Silverman, J. D. 2014, ApJS, 214, 15

Steidel, C. C., Adelberger, K. L., Giavalisco, M., Dickinson, M., & Pettini, M. 1999, ApJ, 519, 1

Steidel, C. C., Pettini, M., & Hamilton, D. 1995, AJ, 110, 2519

Straatman, C. M. S., Labbé, I., Spitler, L. R., et al. 2014, ApJ, 783, L14

Szomoru, D., Franx, M., Bouwens, R. J., et al. 2011, ApJ, 735, L22

Takeuchi, T. T., Yoshikawa, K., & Ishii, T. T. 2003, ApJ, 587, L89

Toft, S., van Dokkum, P., Franx, M., et al. 2007, ApJ, 671, 285

van der Wel, A., Franx, M., van Dokkum, P. G., et al. 2014, ApJ, 788, 28

Whitaker, K. E., Franx, M., Leja, J., et al. 2014, ApJ, 795, 104

Williams, R. J., Quadri, R. F., Franx, M., van Dokkum, P., & Labbé, I. 2009, ApJ, 691, 1879

Wittman, D., Bhaskar, R., & Tobin, R. 2016, MNRAS, 457, 4005

Wyder, T. K., Treyer, M. A., Milliard, B., et al. 2005, ApJ, 619, L15

Young, L. M., Bureau, M., Davis, T. A., et al. 2011, MNRAS, 414, 940